BRAIN
A JOURNAL OF NEUROLOGY

Immune cells perturb axons and impair neuronal survival in a mouse model of infantile neuronal ceroid lipofuscinosis

Janos Groh,[1] Thomas G. Kühl,[2] Chi Wang Ip,[1] Hemanth R. Nelvagal,[2] Sarmi Sri,[2] Steven Duckett,[2] Myriam Mirza,[3] Thomas Langmann,[3,4] Jonathan D. Cooper[2] and Rudolf Martini[1]

1 Department of Neurology, Section of Developmental Neurobiology, University of Wuerzburg, Josef-Schneider-Str. 11, D-97080 Wuerzburg, Germany
2 Department of Neuroscience, King's Health Partners Centre for Neurodegeneration Research, Institute of Psychiatry, King's College London, 125 Coldharbour Lane, SE5 9NU London, UK
3 Institute of Human Genetics, University of Regensburg, Franz-Josef-Strauss-Allee 11, D-93053 Regensburg, Germany
4 Centre of Ophthalmology, University Hospital of Cologne, Department of Experimental Immunology of the Eye, Joseph-Stelzmann-Str. 9, D-50931 Cologne, Germany

Correspondence to: Rudolf Martini,
Department of Neurology,
Developmental Neurobiology,
Josef-Schneider-Str. 11,
D-97080 Wuerzburg,
Germany
E-mail: rudolf.martini@mail.uni-wuerzburg.de

Correspondence may also be addressed to: Janos Groh. E-mail: groh_J@klinik.uni-wuerzburg.de

The neuronal ceroid lipofuscinoses are fatal neurodegenerative disorders in which the visual system is affected early in disease progression. A typical accompanying feature is neuroinflammation, the pathogenic impact of which is presently obscure. Here we investigated the role of inflammatory cells in palmitoyl protein thioesterase 1-deficient ($Ppt1^{-/-}$) mice, a model of infantile neuronal ceroid lipofuscinosis (CLN1 disease, infantile), predominantly focusing on the visual system. We detected an early infiltration of CD8 + T-lymphocytes and observed activation of microglia/macrophage-like cells. To analyse the pathogenic impact of lymphocytes, we crossbred $Ppt1^{-/-}$ mice with mutants lacking lymphocytes ($Rag1^{-/-}$), and scored axonal transport, axonal perturbation and neuronal survival. This lack of lymphocytes led to a significant amelioration of disease phenotypes, not only in the retino-tectal system, but also in other regions of the central nervous system. Finally, reconstitution experiments revealed a crucial role of CD8 + T-lymphocytes in pathogenesis. Our study provides novel pathomechanistic insights that may be crucial for developing treatment strategies.

Introduction

The neuronal ceroid lipofuscinoses are a group of fatal inherited lysosomal storage disorders that severely impact the CNS (Kohlschutter *et al.*, 1993). Although the genetic causes have been identified for several forms (Jalanko and Braulke, 2009) and despite gaining some insights into disease mechanisms (Zhang *et al.*, 2006; Ahtiainen *et al.*, 2007), there are currently no effective therapies for these disorders (Cooper, 2008; Wong *et al.*, 2010). Despite their genetic heterogeneity, the neuronal ceroid lipofuscinoses share certain histopathological and clinical characteristics (Cooper, 2010). All forms of neuronal ceroid lipofuscinosis display selective degeneration of CNS neurons and increased accumulation of autofluorescent storage material. Clinically, deterioration of vision is often one of the earliest symptoms, followed by blindness, motor abnormalities, epilepsy, dementia and ultimately premature death (Haltia, 2006).

Infantile neuronal ceroid lipofuscinosis, or CLN1 disease, infantile, is a severe and early-onset form of neuronal ceroid lipofuscinosis caused by mutations in the *PPT1* (also known as *CLN1*) gene, encoding for palmitoyl-protein thioesterase 1, a soluble lysosomal enzyme. Patients with infantile neuronal ceroid lipofuscinosis develop normally until they become symptomatic at ~12 months of age and usually die by 10 years of age (Santavuori *et al.*, 1973, 1974). The precise function of PPT1 in the CNS is not clear and the primary mechanisms leading to the profound deficits caused by *PPT1* mutations remain poorly understood. A murine model of infantile neuronal ceroid lipofuscinosis, which was generated by disruption of the *Ppt1* gene, mimics the deficits observed in patients with infantile neuronal ceroid lipofuscinosis including early neuropathology in many brain regions, motor abnormalities and spontaneous seizures, and a reduced life span (Gupta *et al.*, 2001; Kielar *et al.*, 2007).

Interestingly, previous studies in this and other neuronal ceroid lipofuscinosis mouse models revealed an early occurrence of innate immune reactions within the brain, which have been proposed but not proven to play a role in the disease (Kielar *et al.*, 2007). An elegant study in a model of Sandhoff disease, another lysosomal storage disorder, has demonstrated that the chemokine macrophage inflammatory protein 1 alpha (now known as CCL3) contributes to the severity of neurodegeneration, most likely by mediating monocyte infiltration (Wu and Proia, 2004).

We have previously demonstrated that in a model of another genetically-caused disease, myelin-related leukodystrophy, low-grade, secondary inflammation substantially contributes to neural damage (Ip *et al.*, 2006). Clonally expanded CD8 + cytotoxic T-lymphocytes were identified as potent mediators of primarily gliogenic neural damage including axon perturbation (Leder *et al.*, 2007; Kroner *et al.*, 2010). Considering the impact of low-grade inflammation in this leukodystrophy model, we asked the question whether similar immune-mediated damage might occur in *Ppt1*-deficient (*Ppt1*$^{-/-}$) mice.

In the present study we show for the first time that *Ppt1*$^{-/-}$ mice display progressive degeneration and loss of retinal ganglion cells that is promoted by effector T-lymphocytes. Moreover, immune cells also influence thalamocortical pathology and the development of clinical features including impaired visual acuity, myoclonic jerks and reduced longevity. These data suggest that limiting lymphocyte inflammation may emerge as a promising treatment approach to foster neuronal survival in infantile neuronal ceroid lipofuscinosis, and possibly in other forms of neuronal ceroid lipofuscinosis.

Materials and methods

Animals

Mice were kept in the animal facility of the Department of Neurology, University of Wuerzburg, under barrier conditions at a constant light–dark cycle of 14 h in the light and 10 h in the dark. To avoid alterations in the light–dark cycle, all animal experiments were performed in the light and at approximately the same hour (before noon). All animal experiments were approved by the Government of Lower Franconia, Germany.

Ppt1-deficient (*Ppt1*$^{-/-}$) mice with disruption of exon 9 (Gupta *et al.*, 2001) were crossbred with *Rag1*-deficient (*Rag1*$^{-/-}$) mice (Mombaerts *et al.*, 1992) according to previously published protocols (Ip *et al.*, 2006). Of note, *Rag1*$^{-/-}$ mice show a normal life span in our animal facility and do not display any neurological abnormalities. *CD4*$^{-/-}$ (Rahemtulla *et al.*, 1991), *CD8*$^{-/-}$ (Fung-Leung *et al.*, 1991) and wild-type mice were used as donors for bone marrow transplantation experiments. All mouse strains were on a uniform C57BL/6 genetic background.

All genotypes were determined by conventional PCR using isolated DNA from tail biopsies following previously published protocols (Gupta *et al.*, 2001; Ip *et al.*, 2006).

We focused our quantitative analyses of mice at different ages on the following CNS regions: retinal ganglion cell layer, optic nerve, laterodorsal thalamic nucleus, the primary visual cortex and somatosensory barrel field cortex, comprising both white and grey matter regions. Additionally, in some investigations, the superior colliculus (Fig. 4A) and the caudate putamen (Supplementary Fig. 1) were analysed.

Histochemistry and immunofluorescence

Retinal ganglion cells were quantified in flat mount preparations. Eyes were dissected, cut, and corneas and lenses were removed before fixation in 4% paraformaldehyde in PBS for 30 min. Flat mounts (four retinal leaves) were stained with 0.1% cresyl violet for 10 min, rinsed, dehydrated and mounted for microscopy. For quantifying Nissl stained retinal ganglion cells, digital images were acquired (inner, middle, outer region of the flattened retina) and the density of retinal ganglion cells was determined. Only cells that were clearly Nissl stained and displayed the typical shape of retinal ganglion cells were counted (Drager and Olsen, 1981). Middle regions of the flattened retinae are shown in the figures. Similarly, Nissl stained neurons in the laterodorsal thalamic nucleus from 3-month-old mice were quantified in 30 μm thick coronal brain sections. For this purpose, three non-adjacent sections per animal were photographed and the Nissl stained cells were related to the analysed area.

Immunohistochemistry against brain-specific homeobox/POU domain protein 3 a (Brn3a, now known as Pou4f1) expressed by retinal ganglion cells was performed on 10 μm thick transverse retina sections using goat anti-mouse Brn3a (1:50, Santa Cruz) antibodies. Digital images of the middle retinal region were acquired and the

number of Brn3a + cells in relation to size of the retinal ganglion cell layer was determined.

Axons in the optic nerve were labelled using mouse anti-mouse neurofilament 68 kDa (1:150, Sigma-Aldrich) antibodies in cross-sections 2 mm caudal to the optic nerve head and images of at least three sections per animal were acquired using identical camera settings. The integrated density of the fluorescent signal was determined using ImageJ software (National Institutes of Health). In brief, images were converted to 32 bit greyscale images and a threshold analysis was applied to define immunoreactive profiles. The integrated density of immunoreactive profiles was determined and related to the signal measured in wild-type sections.

Immunohistochemistry against CD3, CD8, CD4, B220, CD11b, CD68, MHC class I, Caspr2 and SMI32 in optic nerve longitudinal sections was performed as previously described (Ip *et al.*, 2006; Kroner *et al.*, 2010; Ip *et al.*, 2012). Cleaved caspase 3 was detected using rabbit anti-mouse antibodies (1:100, Abcam). Mouse IgG autoantibodies were visualized with rabbit anti-mouse IgG antibodies (1:100, Pierce). Immunopositive profiles were quantified in at least three non-adjacent sections for each animal and related to the total area of these sections. Light and fluorescence microscope images were acquired using an Axiophot 2 microscope (Zeiss) with an attached CCD camera (Visitron Systems). Confocal microscopy was performed using a FluoView FV1000 (Olympus) microscope with corresponding software. Brains were dissected, processed and sectioned as previously described (Kielar *et al.*, 2007). Immunoreactivity against CD68 + microglia/macrophages in the brain was assessed using a semi-automated thresholding image analysis, according to previously published protocols (Kielar *et al.*, 2007). Unbiased stereological quantification of Nissl stained cell profiles in the laterodorsal thalamic nucleus, the primary visual cortex and somatosensory barrel field cortex was performed using StereoInvestigator software (Microbrightfield Inc.), as described previously (Kielar *et al.*, 2007).

Semi-quantitative real-time polymerase chain reaction

Freshly dissected optic nerves were snap frozen in liquid nitrogen, followed by homogenization and isolation of total RNA and protein using TRIzol® reagent (Invitrogen), according to previously published protocols (Groh *et al.*, 2012) and 1 µg of RNA was reverse transcribed in a 100 µl reaction using random hexamer primers (Applied Biosystems). Complementary DNA samples were subsequently analysed as triplicates by semi-quantitative real-time PCR using previously developed TaqMan® assays and TaqMan® universal PCR master mix (Applied Biosystems).

Retrograde labelling of retinal ganglion cells

To study integrity of retinal ganglion neurons via retrograde axonal transport, 1.5 µl of 4% fluorogold (Fluorochrome Inc.) in 0.9% saline were injected into each superior colliculus of both brain hemispheres. Mice were anaesthetized and placed into a stereotactic frame. Using a micro drill (Fine Science Tools) and a syringe pump (Stoelting) injections were made into the superior colliculus at stereotactic coordinates -3.6 mm caudal, -0.6 mm lateral and -1.8 ventral to the bregma. After 6 or 12 days, retinal flat mount preparations were photographed as described and fluorogold-positive profile density was determined by manual counting of fluorescently labelled cells.

Electron microscopy

Optic nerves were prepared for electron microscopy as previously described (Ip *et al.*, 2006). Ultrathin longitudinal and cross-sections were investigated using a ProScan Slow Scan CCD camera mounted to a Leo 906 E electron microscope (Zeiss) and corresponding software iTEM (Soft Imaging System). To quantify axonal spheroids, cross-sections 2 mm caudal to the optic nerve head were analysed and regularly distributed images over the cross-sectional area were taken at a fixed magnification. Using morphological criteria, identified abnormalities (spheroids) were counted and related to the total number of quantified axons. At least 10 images and >1000 axons per animal were analysed.

Immunoelectron microscopy

For immunoelectron microscopy, optic nerves and brains of perfusion fixed mice were embedded in 6% agarose after post-fixation overnight. Vibratome sections (50 µm thick) were cut and free-floating sections were blocked with 1% bovine serum albumin in PBS and incubated with 0.1 M NaIO₃ in PBS and subsequently in 5% dimethyl sulphoxide in PBS. Immunohistochemistry against MHC class I was performed using the same conditions as for fresh-frozen cryosections (see above). After diaminobenzidine staining, the sections were osmificated and processed for light and electron microscopy.

Flow cytometry

Leucocytes were isolated from the spleen and brain as previously described (Ip *et al.*, 2006; Kroner *et al.*, 2010). T-lymphocytes were stained using CD8-PE antibodies, gated and analysed concerning expression of activation markers using CD62L-APC, CD44-PerCP and CD69-FITC antibodies and appropriate isotype controls (BD Biosciences). Cells were analysed using a FACSCalibur with CellQuest software (BD Biosciences).

Bone marrow transplantation

Bone marrow from donor mice was isolated and transferred according to previously published protocols (Ip *et al.*, 2006). $Ppt1^{-/-}Rag1^{-/-}$ and $Ppt1^{+/+}Rag1^{-/-}$ mice were reconstituted at 1 month of age and sacrificed at 3 months of age. Successful chimerism was controlled by flow cytometry of splenocytes and immunohistochemistry on optic nerve sections. Importantly, engraftment of transplanted bone marrow led to a frequency of the respective T-lymphocyte types in the Rag1-deficient host spleen and CNS tissue that was similar to Rag1-positive mice.

Detection of autofluorescent storage material

To detect autofluorescent storage material in retinal ganglion cells or laterodorsal thalamic nucleus neurons, transverse sections of retinae or coronal brain sections were post-fixed using 4% paraformaldehyde in PBS for 10 min. Retinal ganglion cells and laterodorsal thalamic nucleus neurons were labelled using mouse anti-mouse NeuN primary antibodies (1:1000, Millipore) and Cy3-conjugated secondary antibodies. Fluorescence microscopic images of the retinal ganglion cell layer or the laterodorsal thalamic nucleus in at least three sections per animal were acquired with identical settings. Using ImageJ software, a threshold analysis was performed for measuring the area of NeuN immunoreactivity and the area of autofluorescent signal with a GFP filter set. The ratio of autofluorescent area per NeuN+ area in at least

10 neurons per image was determined and related to the mean value obtained from wild-type mice.

Determination of myoclonic jerks

The frequency of myoclonic jerks was observed during the daylight cycle by placing mice individually in a clean cage in a quiet room for a 5 min observation period. During this period an observer unaware of genotype documented all myoclonic jerks according to described criteria (Gupta *et al.*, 2001). $Ppt1^{+/+}Rag1^{+/+}$ (wild-type) and $Ppt1^{+/+}Rag1^{-/-}$ control mice were observed until 15 months of age and did not show any myoclonic jerks until this age (data not shown).

Analysis of visual acuity

Mice at 6 months of age were analysed using an optomotor testing apparatus and the corresponding software (Optomotry; Cerebral Mechanics, Inc.), as previously described (Prusky *et al.*, 2000). Visual acuity was quantified by increasing the spatial frequency of a virtual vertical sine wave grating at 100% contrast until an optokinetic response was no longer induced.

Analysis of longevity

$Ppt1^{-/-}Rag1^{+/+}$ ($Ppt1^{-/-}$) and $Ppt1^{-/-}Rag1^{-/-}$ mice were allowed to age unmanipulated until death; moribund mice were sacrificed. Kaplan–Meier analysis was used to measure cumulative survival and determine differences in lifespan. $Ppt1^{+/+}Rag1^{+/+}$ and $Ppt1^{+/+}Rag1^{-/-}$ control mice were observed until 15 months of age and never died before this age (data not shown).

Statistical analysis

All quantitative data and functional/behavioural analyses were performed by investigators unaware of the genotypes of the respective mice. Shapiro–Wilk tests were used to control for normal distribution. Normally distributed data were compared using the unpaired two-tailed Student's *t*-test. Statistical analyses of electron microscopic quantifications were performed by use of the non-parametric Mann–Whitney *U*-test. For multiple comparisons, one-way ANOVA followed by Tukey's *post hoc* test was used. Longevity values were compared by Kaplan–Meier analysis. *P*-values considered as significant were indicated by asterisks according to the following scheme: *$P < 0.05$; **$P < 0.01$; ***$P < 0.001$. Significant differences between $Ppt1^{+/+}$ and $Ppt1^{-/-}$ genotypes are indicated above the corresponding bars. Analyses of $Ppt1^{+/-}$ or $Ppt1^{+/+}Rag1^{-/-}$ mice did not display any differences compared with $Ppt1^{+/+}$ mice in all experiments (except the typical lack of lymphocytes in all $Rag1^{-/-}$ genotypes) and are not shown in most of the figures. In addition, heterozygous $Rag1^{+/-}$ mice ($Ppt1^{+/+}Rag1^{+/-}$ or $Ppt1^{-/-}Rag1^{+/-}$) did not show any differences to $Rag1^{+/+}$ mice (wild-type or $Ppt1^{-/-}Rag1^{+/+}$) and are also not shown.

Results

Ppt1-deficient mice display progressive perturbation and loss of retinal ganglion cells

We analysed the neuropathological phenotype of $Ppt1^{-/-}$ mice from 1 to 7 months of age, i.e. at ages covering presymptomatic (1 month), symptomatic (3 and 5 months) and disease end stage (7 months) when the first 20–30% of mice are dying. Cresyl violet staining on flat mounted retinae was performed in wild-type ($Ppt1^{+/+}$) and $Ppt1^{-/-}$ mice at these ages. This analysis revealed a progressively decreased density of Nissl stained retinal ganglion cells (Fig. 1A). Retinal ganglion cell counts were also performed using immunohistochemistry against the transcription factor Brn3a (Galindo-Romero *et al.*, 2011), which has a function in dendritic and cell soma-related stratification of retinal ganglion cells that is not related to disease (Badea *et al.*, 2009). In 5-month-old mice the number of Brn3a+ cells in the ganglion cell layer of transverse sections through retinae from $Ppt1^{-/-}$ mice was significantly reduced (by $37 \pm 1\%$; $n = 4$ per group; $P < 0.001$), compared with wild-type mice (Fig. 1B).

Next, we investigated the integrity of retinal ganglion cells and their axons by retrograde labelling with fluorogold. In 5-month-old $Ppt1^{-/-}$ mice there were significantly fewer fluorogold-labelled retinal ganglion cells after 6 days of retrograde transport (Fig. 1C and D) that could not be ameliorated by extending this survival time up to 12 days, demonstrating a complete block of retrograde transport (not shown). The reduction in retrogradely labelled retinal ganglion cells ($52 \pm 10\%$) was more pronounced than the loss of retinal ganglion cells determined by cresyl violet staining at the same age ($26 \pm 6\%$). This indicates that the impaired retrograde transport cannot solely be explained by loss of retinal ganglion cells, but also reflects perturbed axonal integrity.

As an alternative axonopathic marker, we performed immunohistochemistry using antibodies against non-phosphorylated neurofilaments (SMI32). In optic nerve sections from $Ppt1^{-/-}$ mice, but barely in sections from wild-type mice, intensely labelled SMI32+ axonal spheroids could be detected (Fig. 1E). Counts revealed a progressively increased number of these axonal spheroids in $Ppt1^{-/-}$ mice from 3 months onwards, reflecting on-going damage of retinal ganglion cells (Fig. 1F). Using quantitative neurofilament-based immunofluorescence in cross-sections 2 mm caudal to the optic nerve head, we found that $43 \pm 5\%$ ($n = 4$ per group; $P < 0.01$) of the axonal signal was lost in $Ppt1^{-/-}$ mice (Fig. 1G), supporting our finding of axonal damage in $Ppt1^{-/-}$ mice.

According to our investigations, the putative staging of axon damage might start with swelling and enhanced SMI32-immunoreactivity, followed by disintegration and degeneration (Fig. 2A and B). Electron microscopy of optic nerve sections additionally demonstrated an accumulation of disintegrating mitochondria and other organelles in axonal spheroids (Fig. 2C). Interestingly, the majority of axonal spheroids detected in 5-month-old $Ppt1^{-/-}$ mice was found in the juxtaparanodal domains of the nodes of Ranvier and showed a chiasm-directed orientation. This observation was confirmed by immunohistochemistry against non-phosphorylated neurofilaments in combination with the juxtaparanodal marker Caspr2, showing that $75 \pm 7\%$ ($n = 3$) of the SMI32+ axonal spheroids co-localized with swollen juxtaparanodes and also displayed a chiasm-directed orientation (Fig. 2D). Taken together, these data demonstrate a progressive degeneration of retinal ganglion cells in $Ppt1^{-/-}$ mice, preceded by axon dysfunction and degeneration.
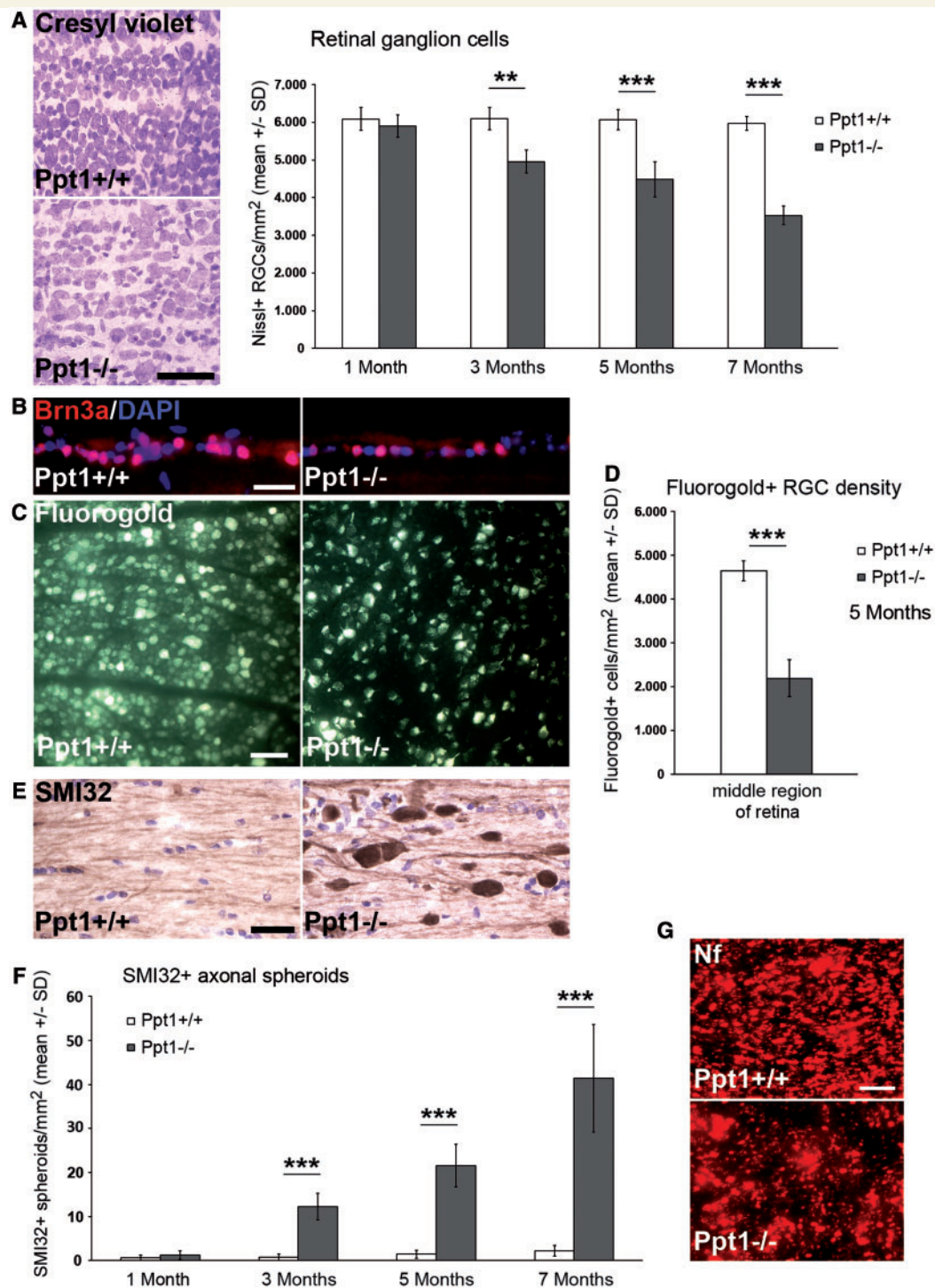
Figure 1 Progressive loss of retinal ganglion cells and axonal degeneration in $Ppt1^{-/-}$ mice. (**A**) Cresyl violet staining of retinal flat mount preparations (at 5 months) and quantification of Nissl + retinal ganglion cells in 1, 3, 5 and 7-month-old $Ppt1^{+/+}$ and $Ppt1^{-/-}$ mice (n = 4–5 per group). Scale bar = 50 μm. (**B**) Brn3a immunohistochemistry on retinal sections from 5-month-old $Ppt1^{+/+}$ and $Ppt1^{-/-}$ mice. Scale bar = 30 μm. Numbers of Brn3a + retinal ganglion cells in $Ppt1^{-/-}$ mice were reduced to 62.8 ± 0.4% of $Ppt1^{+/+}$ mice (n = 4 per group). $P < 0.001$. (**C**) Fluorescence micrographs of retinal flat mount preparations 6 days after injection of fluorogold into the superior colliculus of 5-month-old $Ppt1^{+/+}$ and $Ppt1^{-/-}$ mice. Scale bar = 50 μm. (**D**) Quantification of fluorogold-labelled retinal ganglion cells revealed a significant cell loss in 5-month-old $Ppt1^{-/-}$ compared with $Ppt1^{+/+}$ mice (n = 3 per group). (**E**) Immunohistochemistry using antibodies against non-phosphorylated neurofilaments (SMI32; brownish precipitate) counterstained with haematoxylin (blue) in longitudinal optic nerve section of 7-month-old $Ppt1^{+/+}$ and $Ppt1^{-/-}$ mice. SMI32 + spheroids were often accompanied by numerous cell nuclei. Scale bar = 30 μm. (**F**) Quantification revealed that SMI32 + axonal spheroids are barely detectable in optic nerves of $Ppt1^{+/+}$ mice but accumulated in 3-, 5- and 7-month-old $Ppt1^{-/-}$ mice (n = 4 per group). (**G**) Immunohistochemistry against neurofilaments on optic nerve cross-sections from 7-month-old $Ppt1^{-/-}$ mice demonstrated a reduction of signal to 57.3 ± 4.8% of $Ppt1^{+/+}$ mice (n = 4 per group). $P < 0.01$. Scale bar = 20 μm. Significant differences were determined by Student's t-tests. $**P < 0.01$; $***P < 0.001$. RGC = retinal ganglion cell.
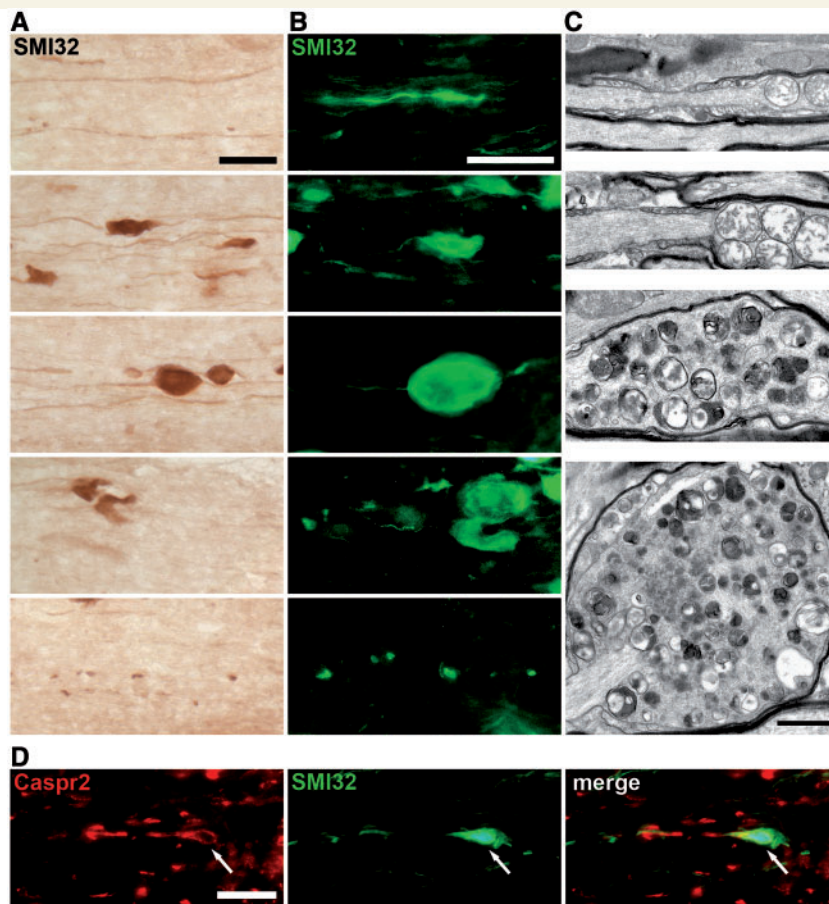
Figure 2 Putative stages of juxtaparanodal axon spheroid formation in *Ppt1*$^{-/-}$ mice. (**A**) Light and (**B**) fluorescence micrographs of putative subsequent stages (*top* to *bottom*) of axonal swelling and degeneration revealed after immunohistochemistry using antibodies against non-phosphorylated neurofilaments on longitudinal optic nerve sections from 5-month-old *Ppt1*$^{-/-}$ mice. Spheroid formation seemed to start with swelling and enhanced SMI32-immunoreactivity, progressively increasing in size and circularity. In some cases, multiple spheroids accumulated along single axons. Large spheroids sometimes appeared to show disintegration and fragmented small immunoreactive remnants oriented in rows might indicate transection, breakdown and degeneration of axons. Scale bars = 30 μm. (**C**) Electron microscopy of longitudinal optic nerve sections from 5-month-old *Ppt1*$^{-/-}$ mice. Mitochondria accumulated in juxtaparanodal spheroids, seemed to disintegrate, and especially in larger spheroids mitochondria seemed to fuse with lysosomes. Other organelles as well as dense bodies also accumulated in axon spheroids. Scale bar = 1 μm. (**D**) Immunohistochemistry against Caspr2 and SMI32 on longitudinal optic nerve sections from 5-month-old *Ppt1*$^{-/-}$ mice demonstrated that spheroids were predominantly (75%) located in the juxtaparanodal domains (arrows). Scale bar = 20 μm. All micrographs are oriented so that the retina is located to the left and the optic chiasm to the right.

CD8+ T-lymphocytes in the central nervous system of *Ppt1*-deficient mice are preferentially attached to axonal spheroids and carry markers of mature effector cells

To investigate cells of the adaptive immune system in the optic nerves of *Ppt1*$^{-/-}$ mice we performed immunohistochemistry against CD3, CD8, CD4 and B220. At all ages investigated, the number of B220+ lymphocytes was low both in wild-type and *Ppt1*$^{-/-}$ mice. Additionally, immunocytochemical studies using antibodies against mouse IgGs failed to provide evidence for a

significant auto-antibody binding to CNS neurons and axons (not shown). Moreover, CD4+ cells were low in number (between 0.66 and 1.38 cells/mm^2 with no significant difference between genotype groups at 1, 3 and 5 months) and there was a small, but significant, increase in their number in *Ppt1*$^{-/-}$ mice, but only at 7 months of age (*Ppt1*$^{+/+}$ mice: 0.87 ± 0.34 cells/mm^2; *Ppt1*$^{-/-}$ mice: 1.87 ± 0.66 cells/mm^2; $n = 4$ per group; $P < 0.05$). In contrast, the number of CD8+ cells was low in wild-type mice, but progressively increased in *Ppt1*$^{-/-}$ mice from 3 months of age onwards (Fig. 3A and C). Notably, in 5-month-old *Ppt1*$^{-/-}$ mice $30 \pm 10\%$ ($n = 4$ per group) of CD8+ cells were in close contact with SMI32+ axonal spheroids and some CD8+ cells showed expression of the major cytotoxic agents perforin and granzyme B (Fig. 3B, Supplementary Fig. 2). The additional immunoreactivity of these cells for CD3 revealed that
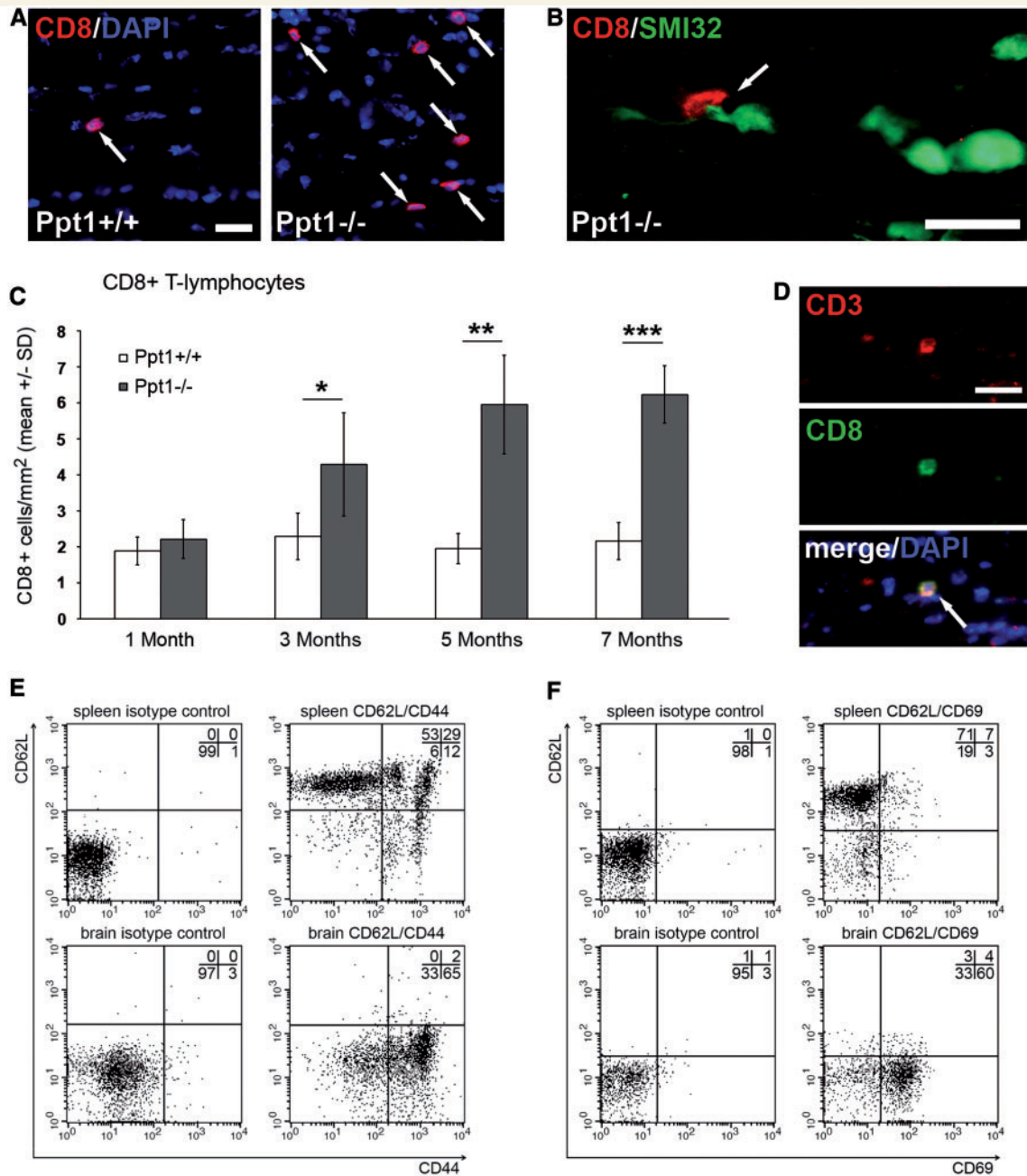
Figure 3 Progressive infiltration of CD8 + effector T-lymphocytes into the CNS of $Ppt1^{-/-}$ mice. (**A**) Immunohistochemical detection of CD8 + cells (arrows) in longitudinal optic nerve sections from 5-month-old $Ppt1^{+/+}$ and $Ppt1^{-/-}$ mice. Scale bar = 30 μm. (**B**) Double immunohistochemistry revealed close contact (arrow) between CD8 + cells and SMI32 + axonal spheroids in $Ppt1^{-/-}$ mice. Scale bar = 30 μm. (**C**) Counts of CD8 + cells revealed their significantly increased number in optic nerves of $Ppt1^{-/-}$ mice compared with $Ppt1^{+/+}$ mice at 3, 5 and 7 months of age (n = 4 per group). Student's t-test. (**D**) Double immunohistochemistry against CD8 and CD3 identified all CD8 + cells in optic nerve sections as T-lymphocytes (arrow). The large majority (∼80%; n = 4 per group at each age) of CD3 + T-lymphocytes were also CD8 + . Scale bar = 30 μm. (**E**) Representative examples of flow cytometry of spleen and brain lymphocytes from $Ppt1^{-/-}$ mice gated for CD8 and analysed for CD62L (marker for immature lymphocytes in this context) and the effector markers CD44 or (**F**) CD69. Left plots show isotype controls and percentages of cells per quadrant are provided in each plot. *$P < 0.05$; **$P < 0.01$; ***$P < 0.001$.

the cells indeed were CD8 + T-lymphocytes and that 78 ± 9% (n = 4 per group) of all T-lymphocytes in the optic nerves of *Ppt1*⁻/⁻ mice were CD8 + at all ages (Fig. 3D). CD8 + T-lymphocytes were also the predominant cells of the adaptive immune system present within the brain of *Ppt1*⁻/⁻ mice from 3 months onwards (Supplementary Fig. 1).

Flow cytometric analyses of freshly isolated brain lymphocytes and splenocytes from 5-month-old *Ppt1*⁻/⁻ mice (n = 3) revealed that 65 ± 9% of the CD8 + T-lymphocytes in the CNS of *Ppt1*⁻/⁻ mice were CD44 + and CD62L− mature effector T-lymphocytes, in contrast with only 12 ± 2% in the spleen (Fig. 3E). While 53.69 ± 3% of the CD8 + T-lymphocytes in the spleen showed a CD62L + and CD44− immature phenotype and 29 ± 2% were double-positive memory T-lymphocytes, CD62L + T-cells were barely detectable in the brains of *Ppt1*⁻/⁻ mice. We obtained similar results using CD69 as another activation marker (Fig. 3F). In comparison, CD8 + cells in the brains of wild-type mice showed lower expression of activation markers (Supplementary Fig. 3). In conclusion, the majority of CD8 + T-lymphocytes in the CNS of *Ppt1*⁻/⁻ mice were mature effector cells expressing markers of activation.

We also investigated the integrity of the blood–brain barrier. Consistent with a recent study (Saha *et al.*, 2012), 7-month-old *Ppt1*⁻/⁻ mice showed a disrupted blood–brain barrier integrity, as reflected by an increased extravasation of blood albumin (Supplementary Fig. 4), whereas extravasation of blood albumin was not detectable in these mice at 5 months and earlier (not shown).

Next, we investigated the expression of major histocompatibility complex class I (MHC class I), the cognate recognition molecule on target structures of CD8 + T-lymphocytes. In the retinal ganglion cell layer, as well as in the optic nerves, and thalamocortical brain regions of *Ppt1*⁻/⁻ mice there was a prominent upregulation of MHC class I immunoreactivity in comparison with wild-type mice, in which MHC class I expression was weak and restricted to perivascular areas (Fig. 4A–C; Supplementary Fig. 5). Double immunohistochemistry demonstrated that some SMI32 + axons in *Ppt1*⁻/⁻ mice showed MHC class I expression, a functional prerequisite for being targeted by CD8 + T-lymphocytes (Fig. 4D). However, large SMI32 + axonal spheroids did not show prominent MHC class I immunoreactivity.

To confirm the surface expression of MHC class I on neurons in *Ppt1*⁻/⁻ mice, we investigated MHC class I expression in plastic embedded material by light microscopy (Fig. 4E), and additionally performed immunoelectron microscopy (Fig. 4F–H). Semi-thin sections of thalamic brain regions revealed numerous MHC class I immunoreactive profiles in *Ppt1*⁻/⁻ mice, which were virtually absent in wild-type mice (Fig. 4E). Using electron microscopy MHC class I expression was detected on the surface and in the endoplasmic reticulum of neuronal somata (Fig. 4F), mostly on cells that contained large amounts of storage material. Moreover, some axons in the optic nerve and synapses in the colliculus superior showed surface expression of MHC class I in *Ppt1*⁻/⁻ mice (Fig. 4G and H). In an individual case, an MHC class I-positive axon was found to be in contact with a non-neuronal cell containing a lytic granule, most likely identifying the cell as an immune-related cell (Fig. 4G). Other cells in the CNS of *Ppt1*⁻/⁻ mice that showed increased MHC class I expression included endothelial cells and microglia/macrophage-like cells (Supplementary Fig. 6A).

Microglia/macrophage-like cells are increased in numbers and activated in the central nervous system of *Ppt1*-deficient mice

Previous studies demonstrated that microglia/macrophage-like cells show elevated expression of F4/80 and morphological signs of activation in the brain of *Ppt1*⁻/⁻ mice when compared with wild-type mice (Kielar *et al.*, 2007). In this study we investigated microglia/macrophages in the optic nerves of *Ppt1*⁻/⁻ mice and wild-type mice at different ages by immunohistochemistry against CD11b. In comparison with wild-type mice, microglia/macrophages in *Ppt1*⁻/⁻ mice showed increased expression of CD11b and 'bushy' cell processes typical of activation (Fig. 5A and B). Quantification revealed significantly increased numbers of CD11b + cells in *Ppt1*⁻/⁻ mice from 3 months of age onwards (Fig. 5C). Similar to the histopathological alterations there was a progressive increase in the number of CD11b + cells in *Ppt1*⁻/⁻ mice until the age of 7 months, the latest time point investigated. Moreover, expression levels of markers of microglial activation, including sialoadhesin, CD16/32 and CD86 (not shown), were upregulated, as well as the neurotoxic cytokines IL-1β and TNFα (Supplementary Fig. 6B). The morphology and number of microglia/macrophages was similar when using other typical microglial markers such as Iba1 or CD68 (Fig. 5D and E). We also identified microglia/macrophages in various regions of the brain, including the laterodorsal thalamic nucleus and primary visual cortex. These studies revealed that microglial activation begins early in disease progression, correlating with the previously published onset of neuron loss (Kielar *et al.*, 2007) (Supplementary Figs 7 and 8).

Lymphocytes impair neuronal survival in *Ppt1*-deficient mice

To investigate the putative pathogenic impact of lymphocytes in *Ppt1*-deficient mice, we crossbred *Ppt1*⁻/⁻ mice with *Rag1*-deficient (*Rag1*⁻/⁻) mice lacking mature T- and B-lymphocytes (Mombaerts *et al.*, 1992) and compared the neuropathological phenotypes of *Ppt1*⁻/⁻*Rag1*⁻/⁻ mice with those seen in single mutants (*Ppt1*⁻/⁻*Rag1*⁺/⁺). As expected, T-lymphocytes were completely absent in the CNS of *Ppt1*⁻/⁻*Rag1*⁻/⁻ mice (not shown). Additionally, there were significantly fewer CD11b + microglia/macrophage-like cells in optic nerves of 5-month-old *Ppt1*⁻/⁻*Rag1*⁻/⁻ mice compared with *Ppt1*⁻/⁻*Rag1*⁺/⁺ mice (Supplementary Fig. 9), whereas the expression of MHC class I was not obviously different (Supplementary Fig. 5). Similarly, thalamocortical microglia/macrophage activation was reduced at this age with less intensely stained CD68 + cells within the thalamus and cortex of *Ppt1*⁻/⁻*Rag1*⁻/⁻ mice (Supplementary Figs 10 and 11).

When we analysed the impact of immune cells on neuronal survival by cresyl violet staining on retinal flat mount preparations, *Ppt1*⁻/⁻*Rag1*⁻/⁻ mice showed a significant attenuation of retinal ganglion cell degeneration at 3, 5 and 7 months of age (Fig. 6A, C and D). Similarly, loss of Brn3a + retinal ganglion cells was significantly attenuated (not shown). These data were supplemented by significantly reduced neuron loss in the thalamus and cortex of
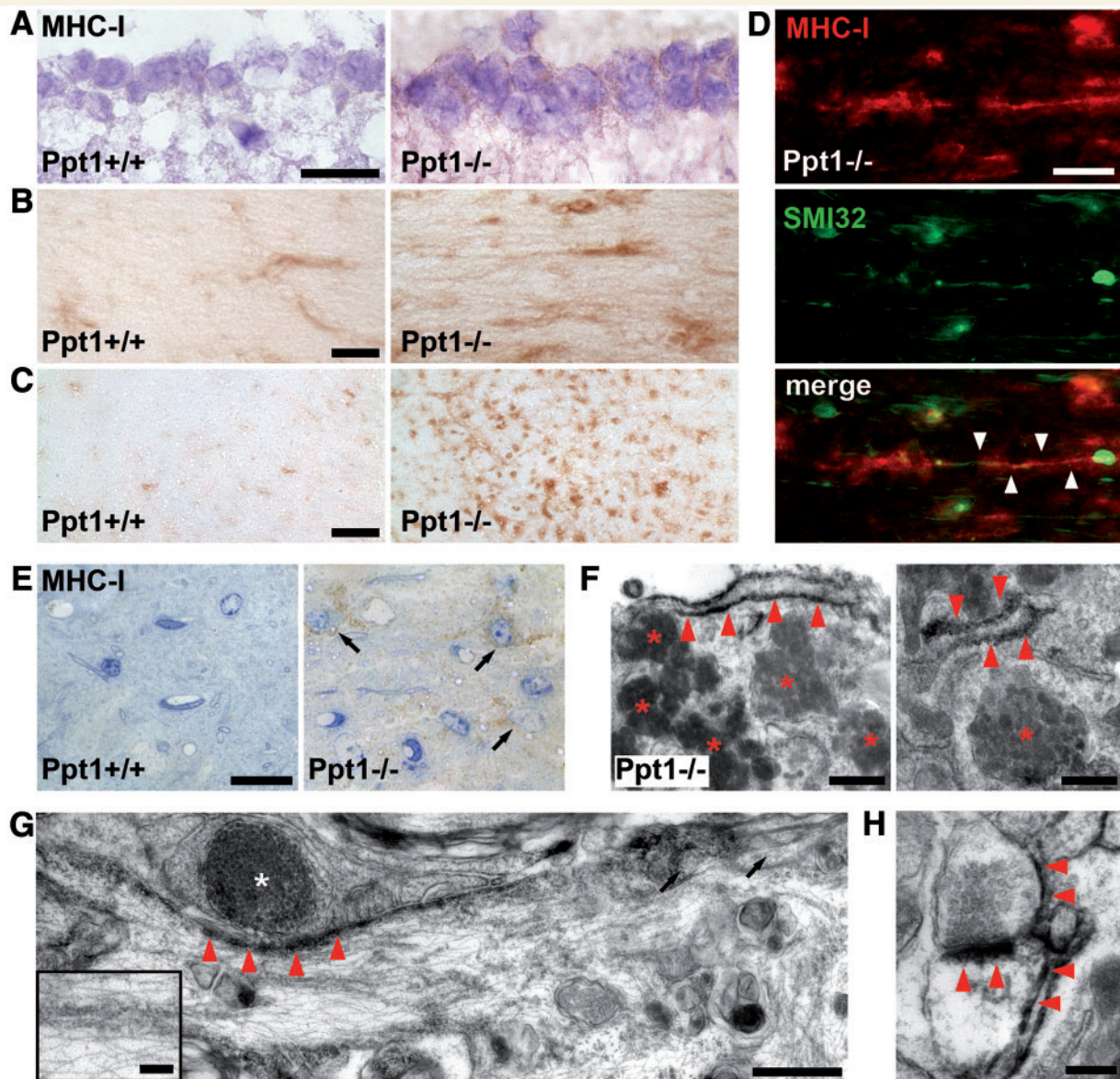
Figure 4 Increased surface expression of MHC class I on neurons in $Ppt1^{-/-}$ mice. (**A**) Immunohistochemical detection of MHC class I (MHC-I, brownish precipitate) in the retinal ganglion cell layer of 5-month-old $Ppt1^{+/+}$ and $Ppt1^{-/-}$ mice counterstained with cresyl violet. Scale bar = 20 μm. (**B**) Immunohistochemical detection of MHC class I in longitudinal optic nerve sections (Scale bar = 30 μm) and (**C**) thalamic brain regions of 5-month-old $Ppt1^{+/+}$ and $Ppt1^{-/-}$ mice. Scale bar = 100 μm. MHC class I expression was weak in the CNS of $Ppt1^{+/+}$ mice and increased in $Ppt1^{-/-}$ mice. (**D**) Double immunohistochemistry using antibodies against MHC class I and SMI32 on longitudinal optic nerve sections from 5-month-old $Ppt1^{-/-}$ mice. Arrowheads demarcate an axon immunoreactive for MHC class I and non-phosphorylated neurofilaments. Scale bar = 30 μm. (**E**) Semi-thin sections of laterodorsal thalamic nucleus after immunolabelling and plastic embedding showed MHC class I + cells (arrows) in 5-month-old $Ppt1^{-/-}$, but barely in $Ppt1^{+/+}$ mice. Scale bar = 20 μm. (**F**) Electron microscopy demonstrated surface expression of MHC class I (dark precipitate; red arrowheads) on neuronal somata in $Ppt1^{-/-}$ mice (*left*). Note the prominent accumulation of storage material in the MHC class I + neuron (red asterisks). Membranes of the endoplasmic reticulum also showed immunoreactivity in some neurons (*right*). Scale bars = 0.5 μm. (**G**) Electron micrograph of an MHC class I + axon in a longitudinal optic nerve section of a 5-month-old $Ppt1^{-/-}$ mouse. Note that the axon is contacted by a cell containing a structure reminiscent of a lytic granule (white asterisk), suggestive for an immune-related cell. Neurofilaments and microtubules as seen at higher magnification (*inset*) and paranodal loops (arrows) of myelinating oligodendrocytes unequivocally identify the MHC class I + structure as an axon. Note that this axon shows features of perturbation as reflected by spheroid formation and disturbed organelles. Scale bar = 0.5 μm; *inset*: 0.1 μm. (**H**) Some pre- and post-synaptic structures in the superior colliculus also showed MHC class I immunoreactivity in $Ppt1^{-/-}$ mice. Scale bar = 0.2 μm.
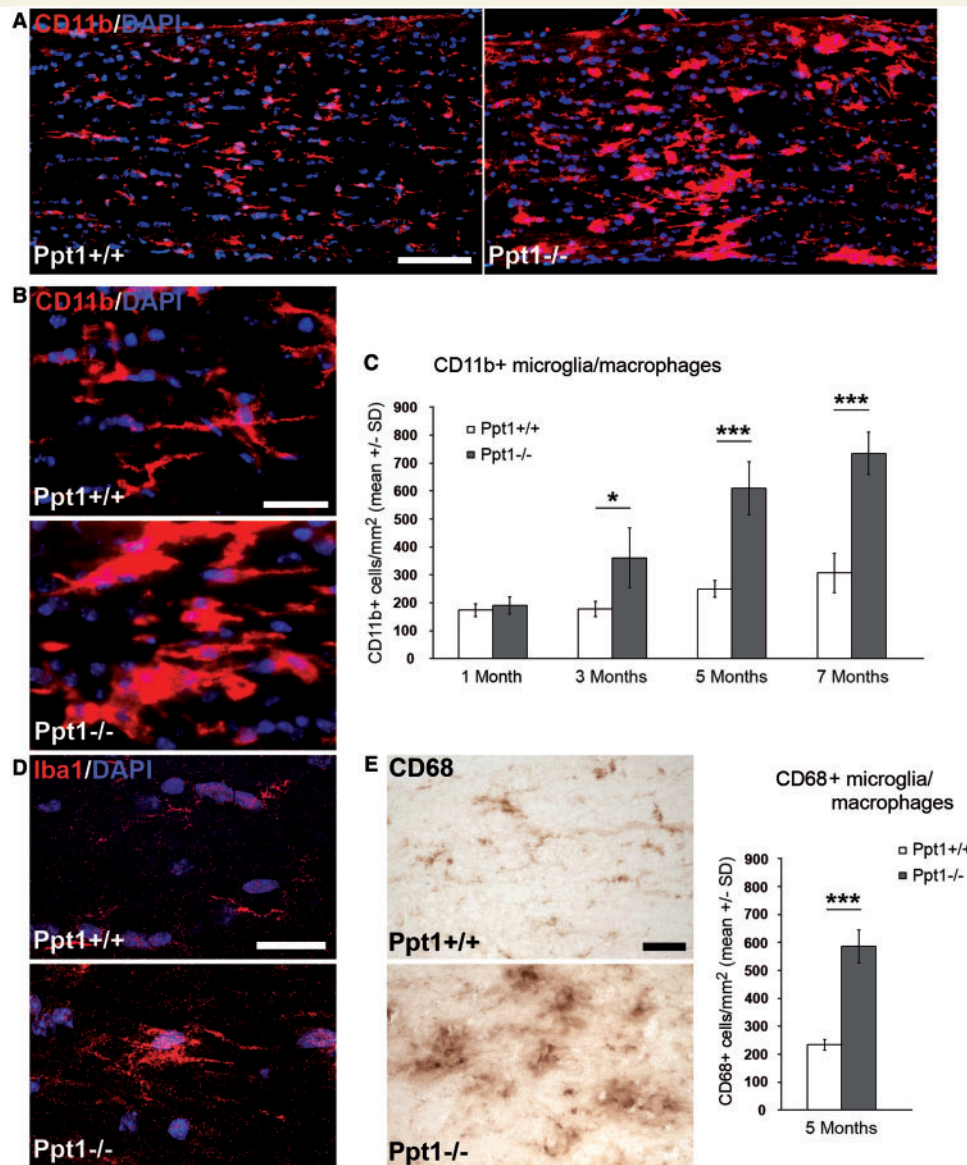
Figure 5 Increased numbers and activation of microglia/macrophage-like cells in the CNS of $Ppt1^{-/-}$ mice. (**A**) Immunohistochemical detection of CD11b + microglia/macrophage-like cells in longitudinal optic nerve sections from 5-month-old $Ppt1^{+/+}$ and $Ppt1^{-/-}$ mice. Scale bar = 100 μm. (**B**) Higher magnification micrographs of CD11b + cell profiles demonstrate increased expression of CD11b and 'bushy' cell processes typical of activation. Scale bar = 30 μm. (**C**) Quantification of CD11b + cells revealed their significantly increased number in $Ppt1^{-/-}$ mice compared with $Ppt1^{+/+}$ mice at 3, 5 and 7 months of age (n = 4–5 per group). Student's t-test. (**D**) Confocal microscopic Z maximum intensity projections (Z mips; five image stack; distance 0.5 μm) of Iba1-labelled microglia/macrophage-like cells confirm 'bushy' morphology in $Ppt1^{-/-}$ mice. Scale bar = 20 μm. (**E**) Light microscopy and quantification of CD68 + microglia/macrophage-like cells (chromogenic detection) in longitudinal optic nerve sections from 5-month-old $Ppt1^{+/+}$ and $Ppt1^{-/-}$ mice reveals comparable morphology and cell numbers as determined using immunofluorescence against CD11b. Scale bar = 30 μm. *$P < 0.05$; ***$P < 0.001$.

$Ppt1^{-/-}Rag1^{-/-}$ mice at 3, 5 and 7 months of age (Figs 6E and 7) and substantial amelioration of the loss of cortical thickness from post-natal month 3 onwards (Supplementary Figs 8 and 11).

To prove that it is the loss of lymphocytes that ameliorates these neurodegenerative phenotypes, we performed bone marrow reconstitution experiments using wild-type mice as donors. The success of this transplantation was controlled by flow cytometry and immunohistochemistry to prove the presence of the respective lymphocyte population in the spleen and CNS. This strategy has

the advantage that the established mouse mutants with an impaired adaptive immune system ($Ppt1^{-/-}Rag1^{-/-}$ mice) are the common 'baseline' for this series of experiments, making the different transplantation procedures directly comparable with each other. Using this approach, reconstitution of the $Ppt1^{-/-}Rag1^{-/-}$ mutants with wild-type bone marrow reversed the $Rag1$-related amelioration at the level of retinal ganglion cell degeneration (Fig. 6B). Similarly, transplantation with bone marrow from $CD4^{-/-}$ donor mice, also reversed the $Rag1$-related amelioration.
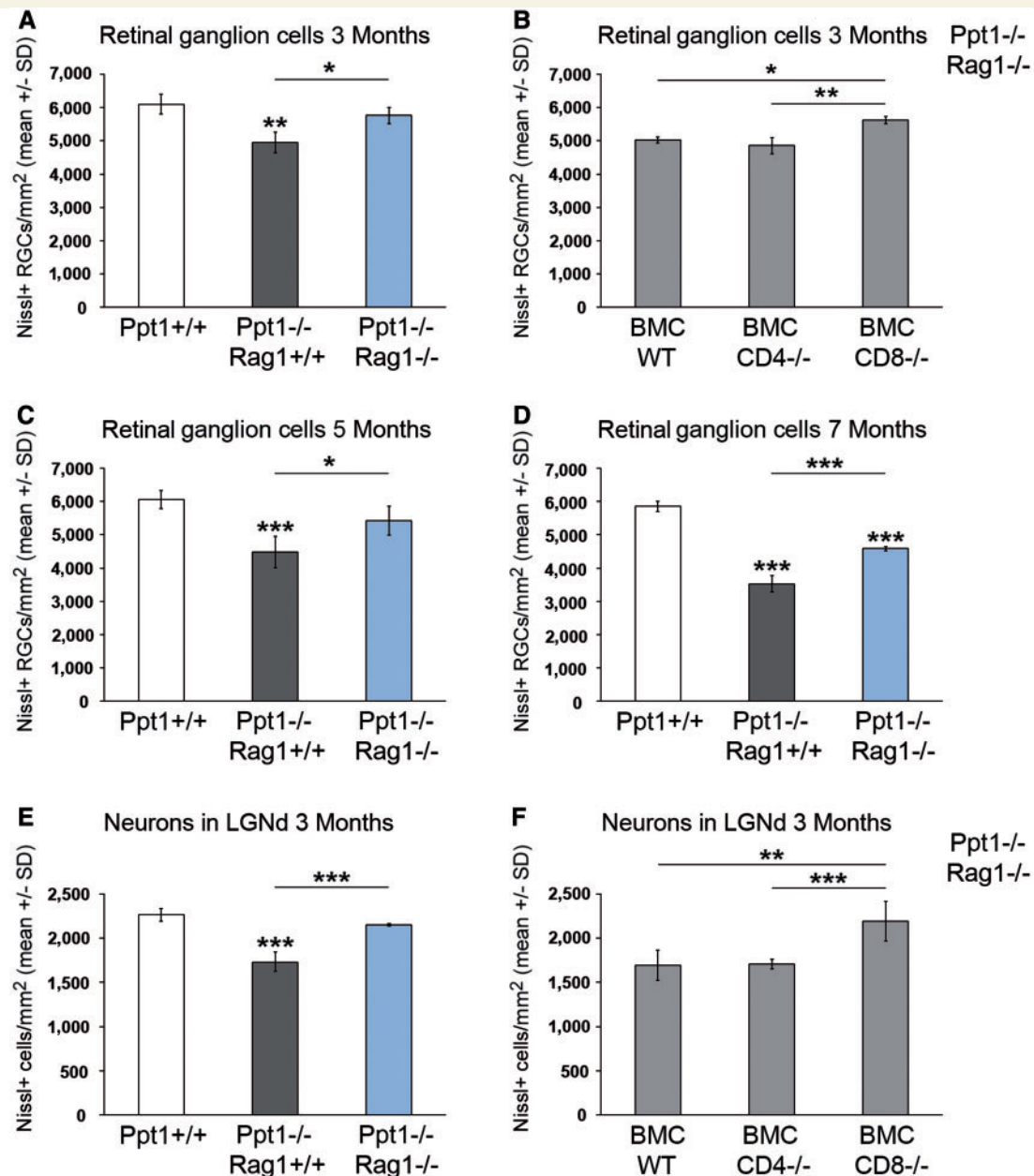
Figure 6 *Rag1* deficiency ameliorates loss of retinal ganglion cells and thalamic neurons in *Ppt1*$^{-/-}$ mice and can be reversed by bone marrow cells from wild-type and *CD4*$^{-/-}$ but not *CD8*$^{-/-}$ mice. (**A**) Quantification of Nissl + retinal ganglion cells after cresyl violet staining of retinal flat mount preparations from 3-month-old *Ppt1*$^{+/+}$, *Ppt1*$^{-/-}$*Rag1*$^{+/+}$ and *Ppt1*$^{-/-}$*Rag1*$^{-/-}$ mice (*n* = 4–5 per group) and (**B**) *Ppt1*$^{-/-}$*Rag1*$^{-/-}$ bone marrow chimeras (BMCs) which received bone marrow from wild-type, *CD4*$^{-/-}$ or *CD8*$^{-/-}$ donor mice (*n* = 4 per group). *Ppt1*$^{-/-}$*Rag1*$^{-/-}$ mice presented with preserved numbers of retinal ganglion cells compared with *Ppt1*$^{-/-}$*Rag1*$^{+/+}$ mice and this effect was abolished by bone marrow cells from wild-type and *CD4*$^{-/-}$ but not *CD8*$^{-/-}$ mice. Quantification of Nissl stained retinal ganglion cells after cresyl violet staining of retinal flat mount preparations from (**C**) 5-month-old and (**D**) 7-month-old *Ppt1*$^{+/+}$, *Ppt1*$^{-/-}$*Rag1*$^{+/+}$ and *Ppt1*$^{-/-}$*Rag1*$^{-/-}$ mice (*n* = 4 per group). (**E**) Quantification of Nissl stained neurons after cresyl violet staining of coronal brain sections in the laterodorsal thalamic nucleus (LGNd) from 3-month-old *Ppt1*$^{+/+}$, *Ppt1*$^{-/-}$*Rag1*$^{+/+}$ and *Ppt1*$^{-/-}$*Rag1*$^{-/-}$ mice (*n* = 3 per group) and (**F**) *Ppt1*$^{-/-}$*Rag1*$^{-/-}$ bone marrow chimeras that received bone marrow from wild-type, *CD4*$^{-/-}$ or *CD8*$^{-/-}$ donor mice (*n* = 4 per group). Significant differences were determined by one-way ANOVA and Tukey's *post hoc* tests. *$P < 0.05$; **$P < 0.01$; ***$P < 0.001$.

In contrast, bone marrow chimeras lacking only CD8 + T-lymphocytes displayed an ameliorated loss of retinal ganglion cells similar to *Ppt1*$^{-/-}$*Rag1*$^{-/-}$ mice (Fig. 6B). Similar observations were also made in the laterodorsal thalamic nucleus (Fig. 6F).

Furthermore, the pronounced reduction in the number of retrogradely labelled retinal ganglion cells in 3-month-old *Ppt1*$^{-/-}$ mice was almost completely prevented by *Rag1* deficiency (Fig. 8A and B). Analysis of cleaved caspase 3, a typical apoptotic marker,
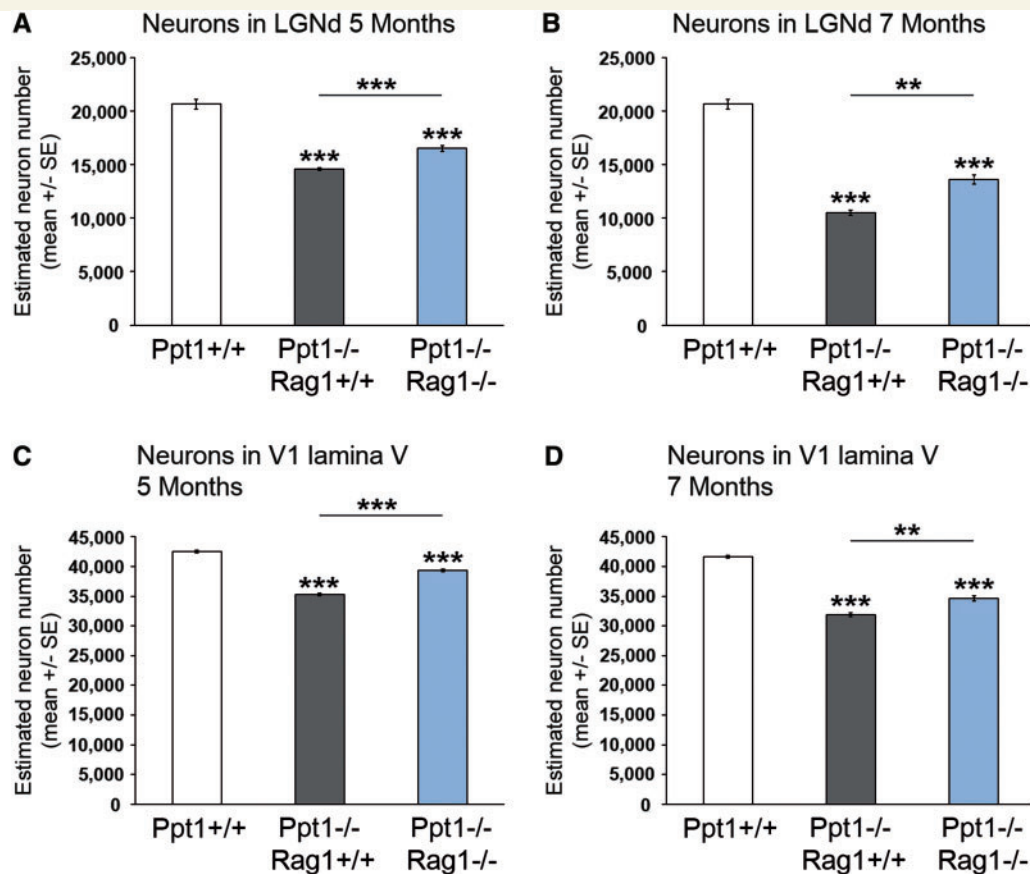
Figure 7 *Rag1* deficiency ameliorates loss of thalamocortical neurons in symptomatic and late-stage *Ppt1*$^{-/-}$ mice. (**A**) Stereological counts of Nissl stained neurons in the laterodorsal thalamic nucleus (LGNd) of *Ppt1*$^{+/+}$, *Ppt1*$^{-/-}$*Rag1*$^{+/+}$ and *Ppt1*$^{-/-}$*Rag1*$^{-/-}$ mice (*n* = 5 per group) at 5 months and (**B**) 7 months of age, as well as in layer V of the primary visual cortex (V1) at (**C**) 5 months and (**D**) 7 months of age displayed a significant amelioration of neurodegeneration in the absence of Rag1. Similar data were obtained for lamina V neuron survival in the somatosensory cortex at 5 months of age (*Ppt*$^{+/+}$ 45 771 ± 1383 neurons; *Rag1*$^{-/-}$ 45 257 ± 964 neurons; *Ppt1*$^{-/-}$ 39 893 ± 1932 neurons; *Ppt1*$^{-/-}$*Rag1*$^{-/-}$ 46 836 ± 684 neurons; *n* = 5 per group. One-way ANOVA and Tukey's *post hoc* tests. **P < 0.01; ***P < 0.001.

demonstrated an increased localisation of this marker in axonal spheroids rather than in the cell soma of retinal ganglion cells, suggesting that the axonal compartment is one of the first targets of the cytotoxic immune cells (Fig. 8C). Cleaved Caspase 3-positive axonal profiles were never seen in wild-type mice (not shown).

Electron microscopic quantification at 3, 5 and 7 months of age also revealed a significantly attenuated formation of axonal spheroids in optic nerve cross-sections from *Ppt1*$^{-/-}$*Rag1*$^{-/-}$ mice, in comparison with sections from *Ppt1*$^{-/-}$*Rag1*$^{+/+}$ mice (Figs 9A, D, 10A and B). Similarly, immunohistochemistry against non-phosphorylated neurofilaments on longitudinal sections confirmed significantly fewer SMI32 + axonal spheroids in the double mutants at 3, 5 and 7 months of age (Figs 9C, F, 10C and D). Corroborating our findings concerning the pathogenic impact of CD8 + T-lymphocytes on neuronal loss, 3-month-old chimeras that received bone marrow from CD8-deficient donor mice showed no difference in the formation of axonal spheroids in comparison with wild-type or *Ppt1*$^{-/-}$*Rag1*$^{-/-}$ mice. In contrast, transplantation of bone marrow from wild-type or CD4-deficient

donor mice reversed the *Rag1*-related attenuation of spheroid formation (Fig. 9B, E and G).

Taken together, we unequivocally demonstrated that CD8 + T-lymphocytes play an important role in disease progression and substantially contribute to neurodegeneration and axon perturbation in *Ppt1*-deficient mice.

Increased accumulation of autofluorescent storage material is a characteristic of infantile neuronal ceroid lipofuscinosis and has been suggested to result from lysosomal dysfunction (Seehafer and Pearce, 2006). To determine whether there was any impact of *Rag1* deficiency on the accumulation of storage material in neurons we performed threshold quantification of autofluorescence in NeuN-labelled retinal ganglion cells and laterodorsal thalamic nucleus neurons. Measuring the total autofluorescence would not be sufficient, because (i) *Ppt1*$^{-/-}$*Rag1*$^{-/-}$ and *Ppt1*$^{-/-}$*Rag1*$^{+/+}$ mice show different densities of neurons owing to their neurodegenerative phenotype; and (ii) micoglia/macrophages with large range of autofluorescence intensity (partially due to different phagocytic activities) would make interpretation of primary
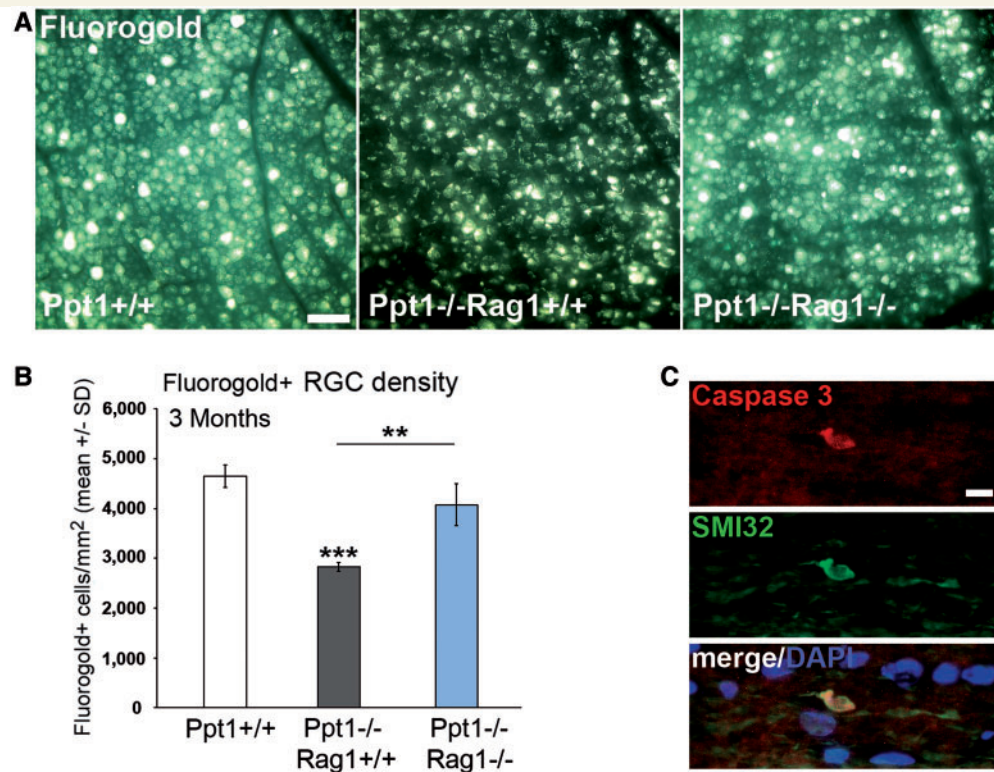
Figure 8 *Rag1* deficiency ameliorates perturbation of retinal ganglion cell axons in *Ppt1*$^{-/-}$ mice. (**A**) Fluorescence micrographs of retinal flat mount preparations 6 days after injection of fluorogold into the superior colliculus of 3-month-old *Ppt1*$^{+/+}$, *Ppt1*$^{-/-}$*Rag1*$^{+/+}$ and *Ppt1*$^{-/-}$*Rag1*$^{-/-}$ mice. Scale bar = 50 μm. (**B**) Quantification of fluorogold-labelled retinal ganglion cells revealed a significant cell loss in 3-month-old *Ppt1*$^{-/-}$*Rag1*$^{+/+}$ compared with *Ppt1*$^{+/+}$ mice, but no difference in retinal ganglion cell numbers in *Ppt1*$^{+/+}$ versus *Ppt1*$^{-/-}$*Rag1*$^{-/-}$ mice (*n* = 3 per group). One-way ANOVA and Tukey's *post hoc* test. (**C**) Immunohistochemical detection of cleaved caspase 3 in combination with SMI32 in longitudinal optic nerve sections from 5-month-old *Ppt1*$^{-/-}$ mice reveals expression in axonal spheroids. Scale bar = 10 μm. **P < 0.01; ***P < 0.001.

neuronal alterations difficult (Fig. 11F). By restricting the measured signal to NeuN + cells in the retinal ganglion cell layer and thalamic laterodorsal thalamic nucleus we measured a >10-fold increase in autofluorescence in 5-month-old *Ppt1*$^{-/-}$ mice compared with wild-type mice (Fig. 11A–F). Importantly, we did not detect any significant difference in autofluorescence in retinal ganglion cells from *Ppt1*$^{-/-}$*Rag1*$^{-/-}$ mice, indicating that *Rag1* deficiency does not alter the generation of the typical storage product in *Ppt1*-deficient neurons (Fig. 11A–F).

Lack of lymphocytes leads to a substantial amelioration of the functional and clinical phenotype and improves longevity of *Ppt1*-deficient mice

To investigate whether there was any functional improvement of the visual system by immune deficiency, we performed optokinetic measurements. At 6 months of age, *Ppt1*-deficient mice showed a significantly decreased visual acuity compared with wild-type mice, consistent with the documented degeneration of retinal

ganglion cells. *Ppt1*$^{-/-}$*Rag1*$^{-/-}$ mice also showed a decreased visual acuity compared with wild-type mice, but a significantly higher visual acuity than *Ppt1*$^{-/-}$*Rag1*$^{+/+}$ mice, demonstrating an amelioration of this functional impairment (Fig. 12A).

We also investigated more general effects of *Rag1* deficiency on the clinical phenotype of *Ppt1*$^{-/-}$ mice. Myoclonic jerks were significantly reduced in 5-month-old double mutants (Fig. 12B). Kaplan–Meier analysis of survival time ultimately demonstrated a significantly increased average lifespan of *Ppt1*$^{-/-}$*Rag1*$^{-/-}$ mice in comparison with *Ppt1*$^{-/-}$*Rag1*$^{+/+}$ mice. While the first *Ppt1*$^{-/-}$*Rag1*$^{+/+}$ mice died at post-natal day 185, *Ppt1*$^{-/-}$*Rag1*$^{-/-}$ mice did not die before day 242 (Fig. 12C). These observations strongly suggest that absence of mature T-lymphocytes leads to a general amelioration of the clinical phenotype and disease severity in *Ppt1*$^{-/-}$ mice.

Discussion

We show for the first time a robust amelioration of axonopathic changes and neuron loss in an animal model of infantile neuronal ceroid lipofuscinosis by genetically inactivating the adaptive immune system. Moreover, by reconstitution of the
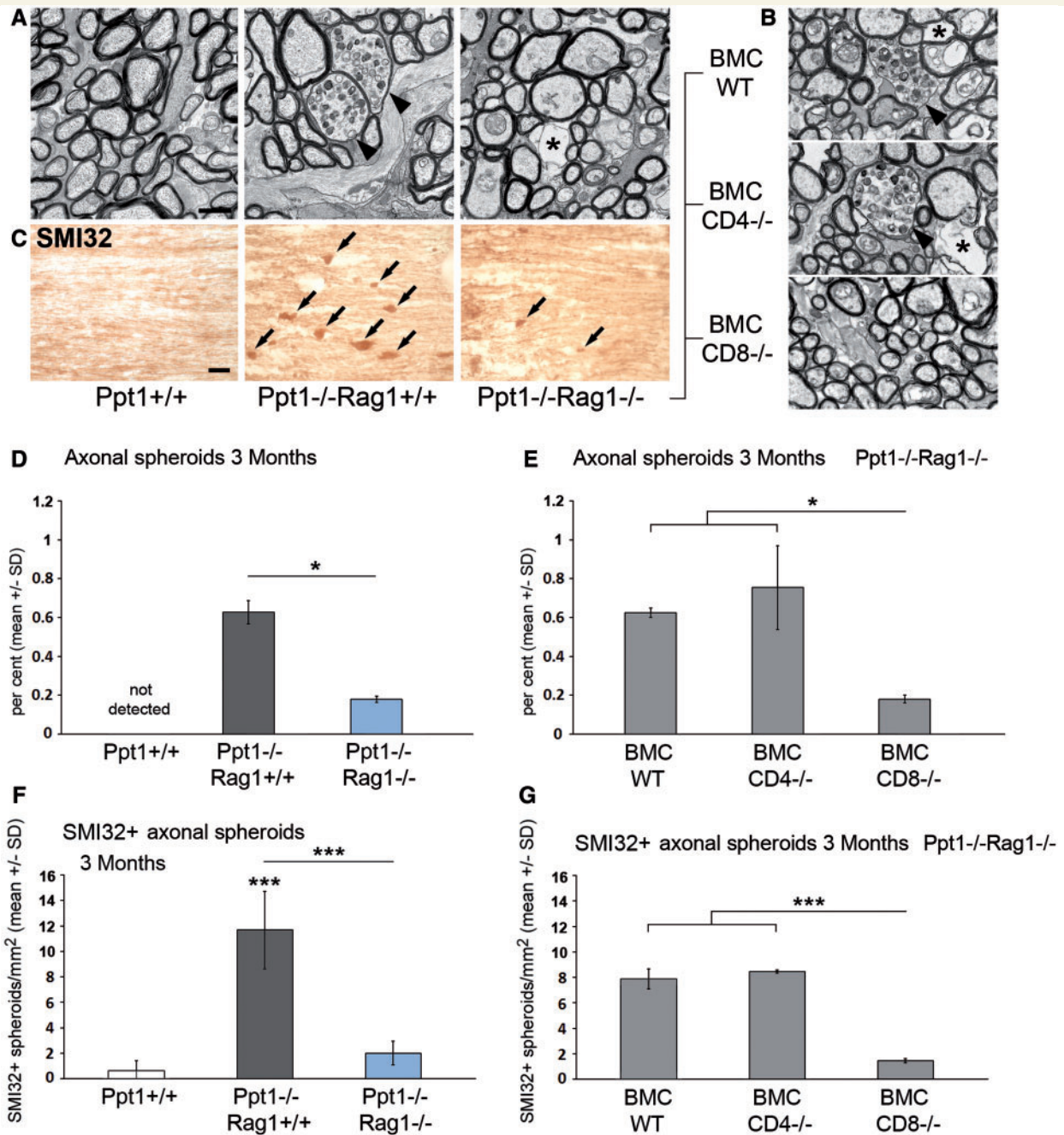
Figure 9 *Rag1* deficiency ameliorates axonal spheroid formation in *Ppt1*^{−/−} mice and can be reversed by bone marrow cells from wild-type and *CD4*^{−/−} but not *CD8*^{−/−} mice. (**A**) Electron micrographs of optic nerve cross-sections from 3-month-old *Ppt1*^{+/+}, *Ppt1*^{−/−}*Rag1*^{+/+} and *Ppt1*^{−/−}*Rag1*^{−/−} mice and (**B**) bone marrow chimeras (BMCs). Axonal spheroids are demarcated by arrowheads. Note the presence of vacuoles (asterisks) in the genotypes deficient for Ppt1, probably indicating storage material removed during the dehydration process. Scale bar = 1 μm. (**C**) Immunohistochemistry using antibodies against non-phosphorylated neurofilaments (SMI32) in longitudinal optic nerve sections from 3-month-old *Ppt1*^{+/+}, *Ppt1*^{−/−}*Rag1*^{+/+} and *Ppt1*^{−/−}*Rag1*^{−/−} mice. Axonal spheroids are marked by arrows. Scale bar = 30 μm. (**D**) Electron microscopic quantification of axonal spheroids in 3-month-old *Ppt1*^{+/+}, *Ppt1*^{−/−}*Rag1*^{+/+} and *Ppt1*^{−/−}*Rag1*^{−/−} mice (*n* = 4–5 per group) and (**E**) bone marrow chimeras (*n* = 4 per group). Spheroid formation was significantly attenuated by *Rag1*-deficiency and this effect was abolished by bone marrow cells from wild-type (WT) and *CD4*^{−/−}, but not *CD8*^{−/−} mice. Bonferroni-corrected Mann-Whitney *U*-tests. (**F**) Quantification of SMI32 + axonal spheroids in 3-month-old *Ppt1*^{+/+}, *Ppt1*^{−/−}*Rag1*^{+/+} and *Ppt1*^{−/−}*Rag1*^{−/−} mice (*n* = 4–5 per group) and (**G**) bone marrow chimeras (*n* = 4 per group). One-way ANOVA and Tukey's *post hoc* tests *$P < 0.05$; ***$P < 0.001$.
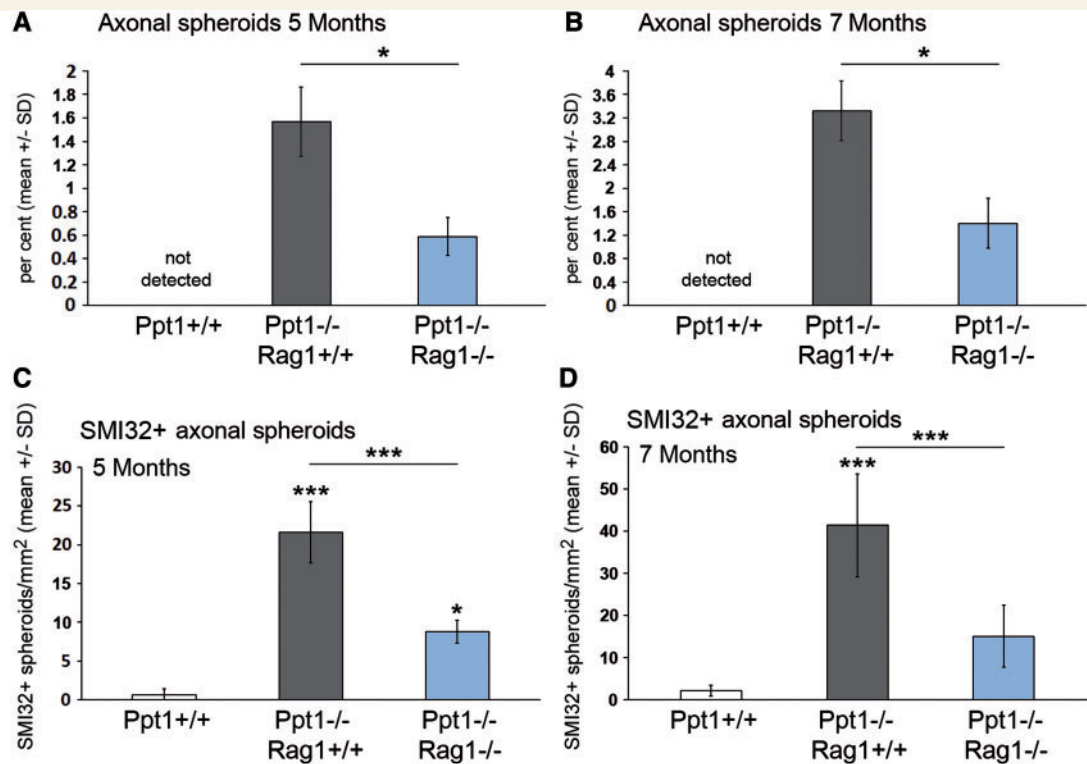
Figure 10 *Rag1* deficiency ameliorates axonal spheroid formation in symptomatic and late-stage *Ppt1*^{-/-} mice. (**A**) Quantification of axonal spheroids in optic nerve cross-sections from 5-month-old and (**B**) 7-month-old *Ppt1*^{+/+}, *Ppt1*^{-/-}*Rag1*^{+/+} and *Ppt1*^{-/-}*Rag1*^{-/-} mice (*n* = 4 per group) by electron microscopy. Mann–Whitney U-test. (**C**) Quantification of axonal spheroids in longitudinal optic nerve sections from 5-month-old and (**D**) 7-month-old *Ppt1*^{+/+}, *Ppt1*^{-/-}*Rag1*^{+/+} and *Ppt1*^{-/-}*Rag1*^{-/-} mice (*n* = 3–4 per group) by immunohistochemistry (SMI32). Note the different scales of the *y*-axes at 5 and 7 months. One-way ANOVA and Tukey's *post hoc* tests. *$P < 0.05$; ***$P < 0.001$.

immune-deficient mutants with bone marrow from specific lymphocytic mutants, CD8 + T-lymphocytes were identified as pathogenic mediators. The absence of these T-lymphocytes led not only to an amelioration of axonal and neuronal degeneration, but this neuronal preservation was also reflected by improved visual acuity, reduced frequency of myoclonic jerks and extended longevity, demonstrating a positive clinical effect of immune cell inactivation. Interestingly, a recent study demonstrated that genetically attenuated astrocyte activation in *Ppt1*^{-/-} mice resulted in an aggravated disease phenotype and the proposed mechanisms included increased immune cell infiltration and cytokine upregulation (Macauley *et al.*, 2011). Indeed we could show that genetic inactivation of lymphocytes substantially attenuates disease, unequivocally defining immune cells as pathogenic mediators. There are also hints that immune components might contribute to the juvenile form of neuronal ceroid lipofuscinosis, because pharmacological and genetic suppression of the immune system moderately improved motor performance in the corresponding mouse model (Seehafer *et al.*, 2011).

Importantly, there is increasing knowledge available of the pathogenic link of other neurodegenerative disorders to inflammation. For example, in Alzheimer's disease, microglial cells appear to play both neuroprotective roles by removing antibody-decorated amyloid-β, but also have aggravating activities owing to

detrimental consequences of cytokine release (Fuhrmann *et al.*, 2010; Glass *et al.*, 2010). Previous studies from our group have demonstrated that secondary inflammation contributes to disease outcome in mouse models with myelin-related mutations in the CNS (Ip *et al.*, 2006), as well as in the PNS (Fischer *et al.*, 2008; Kohl *et al.*, 2010; Groh *et al.*, 2012). Thus, secondary inflammation emerges as a common pathogenetically relevant feature in a wide variety of inherited and spontaneous neurological disorders. Of note, in the present model, for the most time of disease progression, the integrity of the blood–brain barrier appears to remain preserved in *Ppt1*^{-/-} mice, as has been observed in other neuroinflammatory conditions including some leukodystrophic models (Ip *et al.*, 2008) and chronic progressive multiple sclerosis (Lassmann *et al.*, 2012). This may have substantial implications, not only for disease mechanisms, but also for assessing putative therapeutic interventions with regard to the blood–brain barrier permeability of the proposed drugs.

In the present model, we have focused our attention on the visual system for two reasons: first, ophthalmological abnormalities are usually the first clinical signs of the neuronal ceroid lipofuscinoses (Haltia, 2006). Second, the visual system is an ideal structure to investigate disease progression owing to its simple and easily accessible neural components, comprising ganglion cell bodies in the retina, a myelinated pathway and a well-defined synaptic
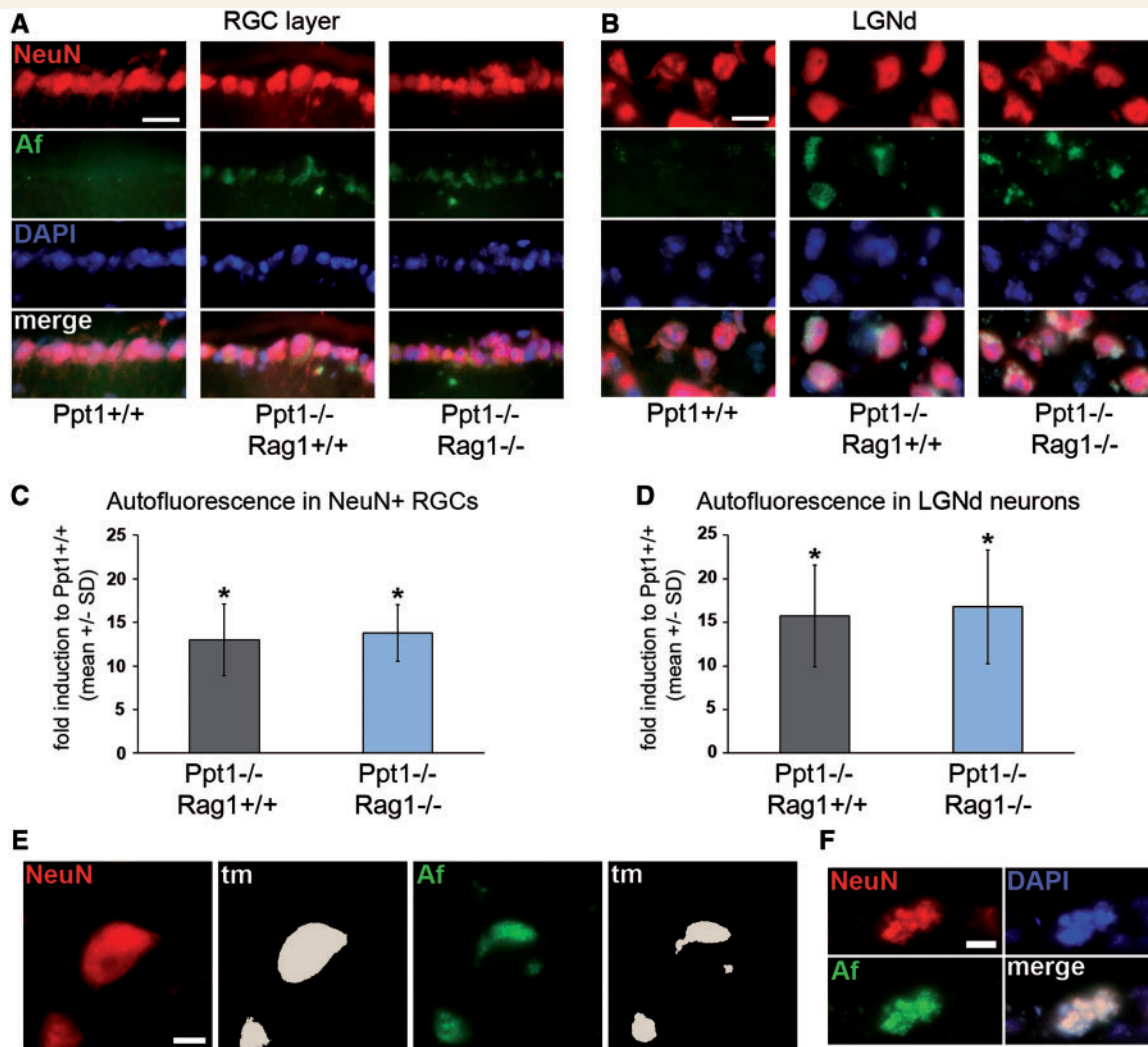
Figure 11 *Rag1* deficiency does not affect the accumulation of autofluorescent storage material in neurons of $Ppt1^{-/-}$ mice. (**A**) Fluorescence micrographs of retinal ganglion cells (RGCs) and (**B**) laterodorsal thalamic nucleus (LGNd) neurons from 5-month-old $Ppt1^{+/+}$, $Ppt1^{-/-}Rag1^{+/+}$ and $Ppt1^{-/-}Rag1^{-/-}$ mice labelled with antibodies against NeuN. Cytoplasmic autofluorescence was detected using a GFP filter set. Af = autofluorescence. Scale bars = 30 μm. (**C**) Threshold analysis of autofluorescence in NeuN + retinal ganglion cells and (**D**) laterodorsal thalamic nucleus neurons demonstrates ∼13- to 16-fold increased accumulation in both $Ppt1^{-/-}Rag1^{+/+}$ and $Ppt1^{-/-}Rag1^{-/-}$ mice in comparison with wild-type mice (n = 3–4 per group). One-way ANOVA and Tukey's *post hoc* test. (**E**) Examples of thresholding analyses for NeuN and autofluorescence signals. Thresholding masks (tm) demarcate positive signals of which the areas were measured. Scale bar = 10 μm. (**F**) Other non-neuronal cells (NeuN negative; probably microglia/macrophage-like cells) also showed prominent accumulation of storage material, but were excluded from analysis. *$P < 0.05$.

projection domain in the superior colliculus. Our findings in this system faithfully reflected the impact of the immune system on different levels of the diseased nervous system, including axon damage, neuronal cell body loss and visual dysfunction in a spatiotemporal manner. By revealing an early morphological and functional impairment of retinal ganglion cells, our study substantially extends the observations made in the $Ppt1^{-/-}$ mutants concerning the cause of visual impairment in infantile neuronal ceroid lipofuscinosis using histopathology and electroretinogram measurements (Griffey *et al.*, 2006). Furthermore, we demonstrate by focusing on axonal transport in the retino-tectal system that axonal damage occurs clearly before substantial loss of neuronal

cell bodies. Accordingly, typical markers of apoptosis were found in degenerating axons. Studies in $Cln3^{-/-}$ mice, a model for the later-onset juvenile neuronal ceroid lipofuscinosis, also indicated degenerative changes in the optic nerve and thalamic projection nuclei rather than in the retina (Weimer *et al.*, 2006). In line with these findings, several studies demonstrated that axonal and synaptic alterations precede the selective loss of neurons, not only in multiple models of neuronal ceroid lipofuscinosis (Kim *et al.*, 2008; Partanen *et al.*, 2008; Kielar *et al.*, 2009), but also in neurological diseases such as multiple sclerosis (Trapp *et al.*, 1998), Alzheimer's disease (Selkoe, 2002), amyotrophic lateral sclerosis (Fischer *et al.*, 2004) and, as a representative of ophthalmic disorders, glaucoma
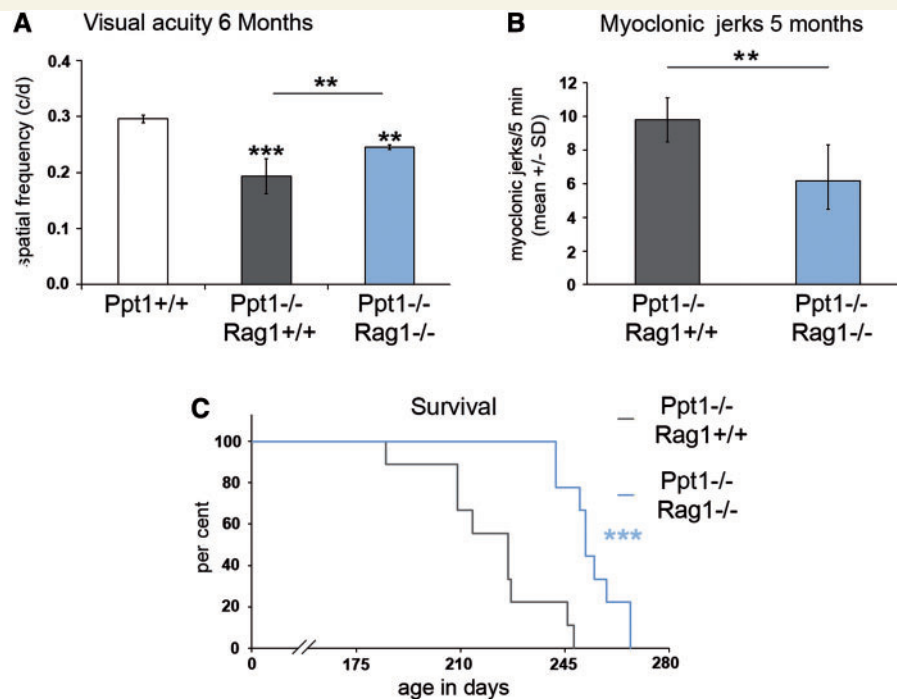
Figure 12 *Rag1* deficiency ameliorates the functional and clinical phenotypes, and improves longevity of *Ppt1⁻/⁻* mice. (**A**) Visual acuity measured by optokinetic responses of 6-month-old *Ppt1⁺/⁺*, *Ppt1⁻/⁻Rag1⁺/⁺* and *Ppt1⁻/⁻Rag1⁻/⁻* mice (n = 4 per group). *Rag1* deficiency significantly improved visual acuity in *Ppt1⁻/⁻* mice. One-way ANOVA and Tukey's *post hoc* test. (**C**) Myoclonic jerks during 5 min observation were significantly less frequent in 5-month-old *Ppt1⁻/⁻Rag1⁻/⁻* than in *Ppt1⁻/⁻Rag1⁺/⁺* mice. Student's *t*-test. (**D**) Kaplan–Meier survival analysis of *Ppt1⁻/⁻Rag1⁺/⁺* and *Ppt1⁻/⁻Rag1⁻/⁻* mice (n = 9 per group) demonstrated improved longevity in the absence of Rag1. **$P < 0.01$; ***$P < 0.001$.

(Buckingham *et al.*, 2008). Thus, our analysis of the retino-tectal system enabled us to identify axon damage as an early, neurodegenerative event, adding to an emerging concept of early axonal damage in many neurodegenerative disorders. It remains to be seen whether it will emerge as a general feature of neurodegenerative disorders that early axonal damage is mediated or amplified by components of the immune system.

Of note, similar to previous studies from our group (Ip *et al.*, 2006; Kroner *et al.*, 2010), CD8+ T-lymphocytes were identified as pathogenic effector cells. Although experimental proof of a substantial implication of CD8+ T-cells has been provided specifically in 3-month-old Ppt1 mutants, there is strong evidence that the pathogenic effect of lymphocytes is also caused by CD8+ cells at older ages. These cells are not only the predominant lymphocyte population in the CNS, but they steadily increase in number and predominance with disease progression. Moreover, at ages older than 3 months, our fluorescent and confocal microscopic studies clearly demonstrated that CD8+ cells are preferentially in close contact to damaged axonal structures, which are strongly reduced in size and number in the absence of lymphocytes. Lastly, our immunocytochemical studies also showed that, at older ages, these CD8+ cells express the major cytotoxic agents perforin and granzyme B. In contrast with our previous studies in myelin mutant mice, *Ppt1*-deficient neurons rather than oligodendrocytes might be the targets of CD8+ T-lymphocytes. This hypothesis is supported by the increased expression of MHC class I on neurons

and, as mentioned above, that CD8+ T cells were spatially associated with small SMI32+ axonal spheroids. The fact that damage was predominantly located at the juxtaparanodal domains of the node of Ranvier in this and other disease models unrelated to neuronal ceroid lipofuscinosis (Ip *et al.*, 2012) potentially defines this region as a new 'hot spot' for immune-mediated axonopathy.

How mutations in a gene encoding for a lysosomal enzyme lead to recruitment of inflammatory cells is currently not clear. The accumulation of storage material may cause distinct forms of cellular stress (Zhang *et al.*, 2006; Ahtiainen *et al.*, 2007; Wei *et al.*, 2008) possibly resulting in the expression of MHC class I molecules on prospective target cells and the upregulation of proinflammatory cytokines as shown in this study and in cultured astrocytes from *Ppt1⁻/⁻* mice (Saha *et al.*, 2008). Importantly, our study showed that the accumulation of storage material alone does not stringently cause immediate neurodegeneration, as we demonstrated in the retino-tectal system, where neuronal integrity and function can be preserved for a significant time period by silencing the adaptive immune system. Interestingly, we show that these beneficial effects of immune depletion do not only occur in the retino-tectal system, but also in other brain regions. These observations not only reflect the prominent pathogenic role of the immune system in the CNS of infantile neuronal ceroid lipofuscinosis mice, but also point to the possibility that the retino-tectal system may be viewed as a reliable surrogate tissue for evaluating disease progression and possible therapeutic

effects in future treatment approaches by using modern imaging techniques, such as optic coherence tomography.

We show that genetic inactivation of CNS-infiltrating CD8 + T-lymphocytes ameliorates all the investigated disease phenotypes in a model for infantile neuronal ceroid lipofuscinosis, a non-treatable fatal genetic disease, with a high disease-modifying impact in many regions of the diseased CNS. Considering that T-lymphocytes are identified as potent contributors to neurodegeneration in models of infantile neuronal ceroid lipofuscinosis, there is emerging hope that novel treatment approaches with blood–brain barrier permeable immune modulators might be designed to foster neuronal survival and improve clinical outcome by attenuating inflammation in various forms of neuronal ceroid lipofuscinosis.

Acknowledgements

Funding

Supplementary material

Supplementary material is available at *Brain* online.

References

Ahtiainen L, Kolikova J, Mutka AL, Luiro K, Gentile M, Ikonen E, et al. Palmitoyl protein thioesterase 1 (Ppt1)-deficient mouse neurons show alterations in cholesterol metabolism and calcium homeostasis prior to synaptic dysfunction. Neurobiol Dis 2007; 28: 52–64.

Badea TC, Cahill H, Ecker J, Hattar S, Nathans J. Distinct roles of transcription factors brn3a and brn3b in controlling the development, morphology, and function of retinal ganglion cells. Neuron 2009; 61: 852–64.

Buckingham BP, Inman DM, Lambert W, Oglesby E, Calkins DJ, Steele MR, et al. Progressive ganglion cell degeneration precedes neuronal loss in a mouse model of glaucoma. J Neurosci 2008; 28: 2735–44.

Cooper JD. Moving towards therapies for juvenile Batten disease? Exp Neurol 2008; 211: 329–31.

Cooper JD. The neuronal ceroid lipofuscinoses: the same, but different? Biochem Soc Trans 2010; 38: 1448–52.

Drager UC, Olsen JF. Ganglion cell distribution in the retina of the mouse. Invest Ophthalmol Vis Sci 1981; 20: 285–93.

Fischer LR, Culver DG, Tennant P, Davis AA, Wang M, Castellano-Sanchez A, et al. Amyotrophic lateral sclerosis is a distal axonopathy: evidence in mice and man. Exp Neurol 2004; 185: 232–40.

Fischer S, Kleinschnitz C, Muller M, Kobsar I, Ip CW, Rollins B, et al. Monocyte chemoattractant protein-1 is a pathogenic component in a model for a hereditary peripheral neuropathy. Mol Cell Neurosci 2008; 37: 359–66.

Fuhrmann M, Bittner T, Jung CK, Burgold S, Page RM, Mitteregger G, et al. Microglial Cx3cr1 knockout prevents neuron loss in a mouse model of Alzheimer's disease. Nat Neurosci 2010; 13: 411–3.

Fung-Leung WP, Schilham MW, Rahemtulla A, Kundig TM, Vollenweider M, Potter J, et al. CD8 is needed for development of cytotoxic T cells but not helper T cells. Cell 1991; 65: 443–9.

Galindo-Romero C, Aviles-Trigueros M, Jimenez-Lopez M, Valiente-Soriano FJ, Salinas-Navarro M, Nadal-Nicolas F, et al. Axotomy-induced retinal ganglion cell death in adult mice: quantitative and topographic time course analyses. Exp Eye Res 2011; 92: 377–87.

Glass CK, Saijo K, Winner B, Marchetto MC, Gage FH. Mechanisms underlying inflammation in neurodegeneration. Cell 2010; 140: 918–34.

Griffey MA, Wozniak D, Wong M, Bible E, Johnson K, Rothman SM, et al. CNS-directed AAV2-mediated gene therapy ameliorates functional deficits in a murine model of infantile neuronal ceroid lipofuscinosis. Mol Ther 2006; 13: 538–47.

Groh J, Weis J, Zieger H, Stanley ER, Heuer H, Martini R. Colony-stimulating factor-1 mediates macrophage-related neural damage in a model for Charcot-Marie-Tooth disease type 1X. Brain 2012; 135: 88–104.

Gupta P, Soyombo AA, Atashband A, Wisniewski KE, Shelton JM, Richardson JA, et al. Disruption of PPT1 or PPT2 causes neuronal ceroid lipofuscinosis in knockout mice. Proc Natl Acad Sci USA 2001; 98: 13566–71.

Haltia M. The neuronal ceroid-lipofuscinoses: from past to present. Biochim Biophys Acta 2006; 1762: 850–6.

Ip CW, Kohl B, Kleinschnitz C, Reuss B, Nave KA, Kroner A, et al. Origin of CD11b + macrophage-like cells in the CNS of PLP-overexpressing mice: low influx of haematogenous macrophages and unchanged blood-brain-barrier in the optic nerve. Mol Cell Neurosci 2008; 38: 489–94.

Ip CW, Kroner A, Bendszus M, Leder C, Kobsar I, Fischer S, et al. Immune cells contribute to myelin degeneration and axonopathic changes in mice overexpressing proteolipid protein in oligodendrocytes. J Neurosci 2006; 26: 8206–16.

Ip CW, Kroner A, Groh J, Huber M, Klein D, Spahn I, et al. Neuroinflammation by cytotoxic T-lymphocytes impairs retrograde axonal transport in an oligodendrocyte mutant mouse. PLoS One 2012; 7: e42554.

Jalanko A, Braulke T. Neuronal ceroid lipofuscinoses. Biochim Biophys Acta 2009; 1793: 697–709.

Kielar C, Maddox L, Bible E, Pontikis CC, Macauley SL, Griffey MA, et al. Successive neuron loss in the thalamus and cortex in a mouse model of infantile neuronal ceroid lipofuscinosis. Neurobiol Dis 2007; 25: 150–62.

Kielar C, Wishart TM, Palmer A, Dihanich S, Wong AM, Macauley SL, et al. Molecular correlates of axonal and synaptic pathology in mouse models of Batten disease. Hum Mol Genet 2009; 18: 4066–80.

Kim SJ, Zhang Z, Sarkar C, Tsai PC, Lee YC, Dye L, et al. Palmitoyl protein thioesterase-1 deficiency impairs synaptic vesicle recycling at nerve terminals, contributing to neuropathology in humans and mice. J Clin Invest 2008; 118: 3075–86.

Kohl B, Fischer S, Groh J, Wessig C, Martini R. MCP-1/CCL2 modifies axon properties in a PMP22-overexpressing mouse model for Charcot-Marie-Tooth 1A neuropathy. Am J Pathol 2010; 176: 1390–9.

Kohlschutter A, Gardiner RM, Goebel HH. Human forms of neuronal ceroid-lipofuscinosis (Batten disease): consensus on diagnostic criteria, Hamburg 1992. J Inherit Metab Dis 1993; 16: 241–4.

Kroner A, Ip CW, Thalhammer J, Nave KA, Martini R. Ectopic T-cell specificity and absence of perforin and granzyme B alleviate neural damage in oligodendrocyte mutant mice. Am J Pathol 2010; 176: 549–55.

Lassmann H, van Horssen J, Mahad D. Progressive multiple sclerosis: pathology and pathogenesis. Nat Rev Neurol 2012; 8: 647–56.

Leder C, Schwab N, Ip CW, Kroner A, Nave KA, Dornmair K, et al. Clonal expansions of pathogenic CD8+ effector cells in the CNS of myelin mutant mice. Mol Cell Neurosci 2007; 36: 416–24.

Macauley SL, Pekny M, Sands MS. The role of attenuated astrocyte activation in infantile neuronal ceroid lipofuscinosis. J Neurosci 2011; 31: 15575–85.

Mombaerts P, Iacomini J, Johnson RS, Herrup K, Tonegawa S, Papaioannou VE. RAG-1-deficient mice have no mature B and T lymphocytes. Cell 1992; 68: 869–77.

Partanen S, Haapanen A, Kielar C, Pontikis C, Alexander N, Inkinen T, et al. Synaptic changes in the thalamocortical system of cathepsin D-deficient mice: a model of human congenital neuronal ceroid-lipofuscinosis. J Neuropathol Exp Neurol 2008; 67: 16–29.

Prusky GT, West PW, Douglas RM. Behavioral assessment of visual acuity in mice and rats. Vision Res 2000; 40: 2201–9.

Rahemtulla A, Fung-Leung WP, Schilham MW, Kundig TM, Sambhara SR, Narendran A, et al. Normal development and function of CD8+ cells but markedly decreased helper cell activity in mice lacking CD4. Nature 1991; 353: 180–4.

Saha A, Kim SJ, Zhang Z, Lee YC, Sarkar C, Tsai PC, et al. RAGE signaling contributes to neuroinflammation in infantile neuronal ceroid lipofuscinosis. FEBS Lett 2008; 582: 3823–31.

Saha A, Sarkar C, Singh SP, Zhang Z, Munasinghe J, Peng S, et al. The blood-brain barrier is disrupted in a mouse model of infantile neuronal ceroid lipofuscinosis: amelioration by resveratrol. Hum Mol Genet 2012; 21: 2233–44.

Santavuori P, Haltia M, Rapola J, Raitta C. Infantile type of so-called neuronal ceroid-lipofuscinosis. 1. A clinical study of 15 patients. J Neurol Sci 1973; 18: 257–67.

Santavuori P, Haltia M, Rapola J. Infantile type of so-called neuronal ceroid-lipofuscinosis. Dev Med Child Neurol 1974; 16: 644–53.

Seehafer SS, Pearce DA. You say lipofuscin, we say ceroid: defining autofluorescent storage material. Neurobiol Aging 2006; 27: 576–88.

Seehafer SS, Ramirez-Montealegre D, Wong AM, Chan CH, Castaneda J, Horak M, et al. Immunosuppression alters disease severity in juvenile Batten disease mice. J Neuroimmunol 2011; 230: 169–72.

Selkoe DJ. Alzheimer's disease is a synaptic failure. Science 2002; 298: 789–91.

Trapp BD, Peterson J, Ransohoff RM, Rudick R, Mork S, Bo L. Axonal transection in the lesions of multiple sclerosis. N Engl J Med 1998; 338: 278–85.

Wei H, Kim SJ, Zhang Z, Tsai PC, Wisniewski KE, Mukherjee AB. ER and oxidative stresses are common mediators of apoptosis in both neurodegenerative and non-neurodegenerative lysosomal storage disorders and are alleviated by chemical chaperones. Hum Mol Genet 2008; 17: 469–77.

Weimer JM, Custer AW, Benedict JW, Alexander NA, Kingsley E, Federoff HJ, et al. Visual deficits in a mouse model of Batten disease are the result of optic nerve degeneration and loss of dorsal lateral geniculate thalamic neurons. Neurobiol Dis 2006; 22: 284–93.

Wong AM, Rahim AA, Waddington SN, Cooper JD. Current therapies for the soluble lysosomal forms of neuronal ceroid lipofuscinosis. Biochem Soc Trans 2010; 38: 1484–8.

Wu YP, Proia RL. Deletion of macrophage-inflammatory protein 1 alpha retards neurodegeneration in Sandhoff disease mice. Proc Natl Acad Sci USA 2004; 101: 8425–30.

Zhang Z, Lee YC, Kim SJ, Choi MS, Tsai PC, Xu Y, et al. Palmitoyl-protein thioesterase-1 deficiency mediates the activation of the unfolded protein response and neuronal apoptosis in INCL. Hum Mol Genet 2006; 15: 337–46.